

11-15
338 603

TECHNICAL NOTE

D-968

CHARTS DEPICTING KINEMATIC AND HEATING PARAMETERS
FOR A BALLISTIC REENTRY AT SPEEDS OF
26,000 TO 45,000 FEET PER SECOND

By Uriel M. Lovelace

Langley Research Center
Langley Air Force Base, Va.

NATIONAL AERONAUTICS AND SPACE ADMINISTRATION
WASHINGTON

October 1961

NATIONAL AERONAUTICS AND SPACE ADMINISTRATION

TECHNICAL NOTE D-968

CHARTS DEPICTING KINEMATIC AND HEATING PARAMETERS

FOR A BALLISTIC REENTRY AT SPEEDS OF

26,000 TO 45,000 FEET PER SECOND

By Uriel M. Lovelace

SUMMARY

Reentry trajectories, including computations of convective and radiative stagnation-point heat transfer, have been calculated by using equations for a point-mass reentry vehicle entering the atmosphere of a rotating, oblate earth. Velocity was varied from 26,000 to 45,000 feet per second; reentry angle, from the skip limit to -20° ; ballistic drag parameter, from 50 to 200. Initial altitude was 400,000 feet. Explicit results are presented in charts which were computed for an initial latitude of 38° N and an azimuth of 90° from north. A method is presented whereby these results may be made valid for a range of initial latitude and azimuth angles.

INTRODUCTION

The reentry phase of spacecraft flight is one of the most difficult design areas the engineer must consider. Since the heating associated with this phase reaches an appreciably great magnitude, it will, in most cases, dictate the design of the reentry configuration. The aerodynamic loads or decelerations are also important parameters that enter the design considerations of a supercircular velocity reentry vehicle.

For many space missions it is desirable and possible to use a ballistic reentry mode for return of the spacecraft to earth; this is particularly true for unmanned vehicles. Approximate solutions are available for descriptions of these parameters in the ballistic reentry. (See refs. 1, 2, and 3, for example.) Exact solutions of the heating equations and equations of motion, however, are more desirable for even general analysis of the reentry problem. Such exact solutions are presented herein.

L
1
7
5
0

Trajectories have been computed on an IBM 7090 electronic data processing system for a two-body system consisting of a point-mass reentry vehicle and a rotating oblate earth. Although the results are limited to particular combinations of azimuths and latitudes, they should be useful for the Wallops Island and Cape Canaveral ranges in that for these latitudes reasonable azimuths may be obtained.

The velocity range considered was from 26,000 to 45,000 feet per second. The reentry angle was varied from near the skip limit to -20° . The ballistic drag parameters considered were 50, 100, and 200. The results are presented in chart form.

SYMBOLS

A	reference area, sq ft
A,B,C	constants
C_D	drag coefficient
F	force, lb
g	gravity, ft/sec ²
h	altitude above reference sphere, ft
L	latitude, deg
m	mass, slugs
Q	total heat input, Btu/ft ²
q	heating rate, Btu/ft ² /sec
\bar{q}	dynamic pressure, $\frac{1}{2}\rho V_a^2$, lb/sq ft
R	radius, ft
R_e	earth's equatorial radius, 20,925,832 ft
R_p	earth's polar radius, 20,854,892 ft
r	radial distance, $R_l + h$, ft
t	time, sec or min

V	velocity, ft/sec
V_s	satellite velocity, ft/sec
W	weight, mg, lb
α	azimuth, deg
γ	flight-path angle, deg
λ	longitude, deg
ρ_o	sea-level density, 2.3769×10^{-3} slug/cu ft
ρ	ambient density, slug/cu ft
σ	range angle, deg
ω_e	earth's rotational speed, $0.729211508 \times 10^{-4}$ radians/sec

Subscripts:

a	relative to a point on the earth
o	initial conditions
c	convective
D	geodetic
e	equatorial
E	easterly component
I	inertial
N	northerly component
n	model nose
P	polar
G	geocentric
R	radiation
r	radial component

4

l local
 L latitudinal component
 λ longitudinal component

A dot over a symbol denotes differentiation with respect to time.

METHOD

The trajectory parameters presented herein were computed on the IBM 7090 digital computer utilizing spherical polar differential equations of motion for a particle near an oblate rotating earth. The computer program was obtained from unpublished data prepared by John N. Shoosmith of the NASA Space Task Group. The following equations describe the accelerations of the vehicle in the longitudinal, latitudinal, and radial directions:

$$\ddot{\lambda} = \frac{1}{r \cos L} \left[\frac{F_{\lambda}}{m} - 2\dot{r}(\dot{\lambda} + \omega_e) \cos L + 2r\dot{L}(\dot{\lambda} + \omega_e) \sin L \right] \quad (1)$$

$$\ddot{L} = \frac{1}{r} \left[\frac{F_L}{m} + g_L - 2\dot{r}\dot{L} - r(\dot{\lambda} + \omega_e)^2 \sin L \cos L \right] \quad (2)$$

$$\ddot{r} = \frac{F_r}{m} + g_r + r\dot{L}^2 + r(\dot{\lambda} + \omega_e)^2 \cos^2 L \quad (3)$$

A more detailed discussion of these equations may be found in reference 4. These equations are not presented exactly as those of reference 4. Since the equations of reference 4 were derived for a stationary earth with a rotating atmosphere and equations (1) to (4) include a rotating earth, the $\dot{\lambda}$ of reference 4 becomes $\dot{\lambda} + \omega_e$ in the rotating-earth situation. The terms and symbols of the equations have been slightly rearranged with no effect on the structure of the derivation. The $\ddot{\lambda}$ equation was not completely differentiated in the reference report but can be readily shown to yield equation (1).

The altitude h in terms of the radial distance r and the local radius R_l is defined as

$$h = r - R_l \quad (4)$$

L
1
7
5
0

where

$$R_L = R_e \left(1 - \frac{1}{2} C \sin^2 L + \frac{3}{8} C^2 \sin^4 L \right) \quad (5)$$

and

$$C = \left(\frac{R_e}{R_p} \right)^2 - 1$$

The following equations define the drag forces acting on the particle in the three aforementioned directions:

$$F_\lambda = -\bar{q} C_D A \left(\frac{V_{aE}}{V_a} \right) \quad (6)$$

$$F_L = -\bar{q} C_D A \left[\frac{V_{aN}}{V_a} \cos(L_D - L_G) + \frac{V_{aR}}{V_a} \sin(L_D - L_G) \right] \quad (7)$$

$$F_R = -\bar{q} C_D A \left[-\frac{V_{aN}}{V_a} \sin(L_D - L_G) + \frac{V_{aR}}{V_a} \cos(L_D - L_G) \right] \quad (8)$$

The easterly, northerly, and radial velocity components of the vehicle or particle are described as

$$V_{aE} = r \dot{\lambda} \cos L \quad (9)$$

$$V_{aN} = r \dot{L} \cos(L_D - L_G) - \dot{r} \sin(L_D - L_G) \quad (10)$$

$$V_{aR} = r \dot{L} \sin(L_D - L_G) + \dot{r} \cos(L_D - L_G) \quad (11)$$

The total velocity, relative to the earth, of the particle along the flight path is defined as

$$V_a = \sqrt{V_{aE}^2 + V_{aN}^2 + V_{aR}^2} \quad (12)$$

The range over the curved earth may be computed from the following equation:

$$\text{Range} = \sigma \left(\frac{R_o + R_l}{2} \right) \quad (13)$$

where

$$\cos \sigma = \sin L_o \sin L + \cos L_o \cos L \cos(\lambda_o - \lambda) \quad (14)$$

The flight-path angle γ_a may be obtained from the relation

$$\sin \gamma_a = \frac{V_{ar}}{V_a} \quad (15)$$

Reference 5 presents the equations for the components of gravity of an oblate earth and the derivation thereof. Reference 6 contains the equations describing the atmospheric properties that define the ARDC 1959 model atmosphere used herein. The approximate convective stagnation heating equations were obtained from reference 7 and are

$$q_c = \frac{17,600}{\sqrt{R_n}} \left(\frac{\rho}{\rho_o} \right)^{1/2} \left(\frac{V_a}{V_s} \right)^{3.15} \quad (16)$$

$$Q_c = \int q_c dt \quad (17)$$

The approximate equations for radiation heating under an equilibrium condition are

$$q_R = AR_n \left(\frac{\rho}{\rho_o} \right)^{1.78} \left(\frac{V_a}{10^4} \right)^3 \quad (18)$$

where

$$A = 0; B = 0 \quad (V_a < 25,000)$$

$$A = 6.8; B = 12.5 \quad (25,000 < V_a < 30,000)$$

$$A = 0.003; B = 19.5 \quad (30,000 < V_a < 35,000)$$

$$A = 20.4; B = 12.5 \quad (35,000 < V_a)$$

and

$$Q_R = \int q_R dt \quad (19)$$

Reference 3 presents a derivation and comparison analysis for equations (18) and (19). The radiative heating rates presented herein have been computed for the stagnation point of a sphere with a radius of 1 foot. In order to correlate these data to a sphere having a nose radius of other than 1 foot, the desired heating rate may be obtained simply by multiplying the rate presented by the nose radius of the specific configuration.

The convective heating rate may be manipulated in much the same way. Again the 1-foot nose radius has been used throughout. For a specific sphere the convective heating rate presented must be divided by the square root of the specific nose radius.

RESULTS AND DISCUSSION

Initial Conditions

The results of the computations are presented in figures 1 to 13 for the range of reentry conditions investigated. The velocity range considered was from 26,000 feet per second to 45,000 feet per second. The ballistic drag parameter $W/C_D A$ range was from 50 to 200. The reentry angle γ_0 was varied from near the skip limit to 20° below the local horizontal. All reentries were initiated at an altitude of 400,000 feet. Both initial conditions and results are presented for earth-relative rather than for inertial conditions.

The results presented herein were computed for a specific initial latitude and azimuth; however, they are not limited to one particular latitude and azimuth. If the inertial velocity, earth-relative velocity, and reentry angle are held constant, the initial azimuth necessary to validate the results presented herein for a chosen latitude, between 0° and 38° north, may be computed. It can be shown that the inertial velocity V_I in terms of the latitude, earth-relative velocity, azimuth, and flight-path angle is

$$V_I^2 = V_a^2 + \omega_e^2 r^2 \cos^2 L + 2\omega_e r V_a \cos L \cos \gamma_a \sin \alpha_a \quad (20)$$

If equation (20) is solved for $\sin \alpha_a$

$$\sin \alpha_a = \frac{V_I^2 - V_a^2 - \omega_e^2 r^2 \cos^2 L}{2V_a \omega_e r \cos L \cos \gamma_a} \quad (21)$$

In order to determine an azimuth for a given latitude, the inertial velocity must be held constant for the initial latitude and for the chosen latitude. Applying equation (20) to the initial conditions and substituting the results into equation (21) yields

$$\sin \alpha_a = \frac{\cos L_0 \sin \alpha_0}{\cos L} + \frac{\omega_{er} \cos^2 L_0}{2V_a \cos L \cos \gamma} - \frac{\omega_{er} \cos L}{2V_a \cos \gamma} \quad (22)$$

Since the results presented herein were computed for a latitude of 38° north and azimuth of 90° from north, equation (22) becomes

$$\sin \alpha_a = \frac{0.78801}{\cos L} + \frac{0.62096 \omega_{er}}{2V_a \cos L \cos \gamma} - \frac{\omega_{er} \cos L}{2V_a \cos \gamma} \quad (23)$$

By choosing a desired latitude, flight-path angle, and earth-relative velocity, equation (23) may be solved for an azimuth necessary to validate these results. Figure 1 shows two curves generated from this equation or the azimuth and latitude relationships for which the results are valid. As can be seen from this chart, reentry angle and velocity have little effect on the azimuth change. The two limits presented are for the two most extreme cases of all those discussed. The lower limit was calculated for an initial velocity of 45,000 feet per second and a reentry angle of 0° (which would not enter but is shown as a limiting case) whereas the upper limit was calculated for an initial velocity of 26,000 feet per second and a reentry angle of -20° .

Skip Limits

The results from the shallow-angle computations defined an approximate skip limit. The skip limit is defined as that reentry angle which, for a particular velocity and W/C_{DA} , results in a trajectory where the reentry vehicle exits from the atmosphere either to escape or to reenter farther downrange and may include additional skips before the final entry. The criterion for determining skip was a trajectory that reached an altitude greater than 400,000 feet after reentry was initiated.

In figure 2 the initial angle γ_0 at which skip occurs is plotted as a function of the reentry velocity for values of W/C_{DA} of 200 and 50.

L
1
7
5
0

The area below these curves is the region where skip will occur. The region above the curves is the region where direct or single pass reentry may be obtained.

Since the accuracy of the skip limit is determined by the number of computations made, no attempt has been made to determine precisely the skip limit in the present analysis. In determining the skip limit no points were computed at intervals less than $\frac{1^\circ}{2}$ in γ_0 . The accuracy of the limit is, therefore, considered to be no better than $\pm\frac{1^\circ}{4}$. Therefore, the data in the charts should be used with caution for reentry angles close to the skip limit defined in figure 2.

Trajectory Profiles

Shown in figure 3 are plots of the variation of altitude with range for initial velocities from 26,000 to 45,000 feet per second. Profiles are given for a range of initial flight-path angles from -20° to a shallow angle close to the skip limit. Also shown are time in seconds from the time of initiation of reentry and velocity at various points along the trajectory. These charts are for a value of W/C_{DA} of 100. Note that, at the steeper reentry angles, the profiles are essentially straight lines down to fairly low altitudes and velocities as predicted in reference 2 whereas, for shallow angles, curvature becomes fairly pronounced at relatively high altitudes and velocities. Figure 3(d) shows that, for $V_0 = 36,000$, $\gamma_0 = -6^\circ$, and $\frac{W}{C_{DA}} = 100$, the reentry angle is close to the skip limit; in fact, for a portion of the trajectory, the reentry vehicle gains altitude. This type of profile is typical for trajectories near the skip limit.

Figure 4 provides a picture of the effect of the variation of W/C_{DA} on the altitude-range profile for specific velocities of 26,000, 36,000, and 45,000 feet per second. The three charts of figure 4 point out the marked effect of W/C_{DA} for shallow reentries. As shown in figures 4(b) and 4(c) the skip may be determined by W/C_{DA} . These charts also point out the relative insignificance of W/C_{DA} variations on the altitude-range profiles at the steeper entry angles. The charts of figures 5 and 6 present curves for the variation of altitude with velocity for initial velocities of 26,000 to 45,000 feet per second. Figure 5 also presents a limited variation of the initial entry angle and ballistic parameter W/C_{DA} for correlation or comparison purposes. In figure 6 the midrange velocity of 36,000 feet per second is considered. In figure 6(a) the entry angle γ_0 was varied from -6°

to -20° . The drag parameter is varied for the two extremes. Figure 6(b) is simply a comparison of the variation of $W/C_D A$ for a velocity of 36,000 feet per second and $\gamma_0 = -10^\circ$. As can be noted from these charts, the higher $W/C_D A$ flight will dip considerably deeper into the velocity altitude corridor than the lower $W/C_D A$ flight.

Range, Time, and Deceleration

The range from initiation of entry to impact is shown in figure 7 as a function of entry angle and entry velocity for the three drag parameters considered. It can be seen that, as the skip limit is approached, the range curves become asymptotic to the entry angle at which skip occurs. Therefore, extreme caution must be exercised in using these charts for ranges greater than 1,000 nautical miles.

A measure of the total time of flight is shown in figure 8. The time of flight shall be defined as the time from initiation of reentry (that is, 400,000 feet) to impact. The curves for all velocities appear to cross near a single point. This apparent crossover is not intended to mean that at this point the time of flight is invariant with velocity, but that these curves have been arbitrarily faired through this point. In order to define the crossover more accurately a large number of computations are necessary. Note that, at shallow reentry angles, the times are becoming very large and therefore the trajectory conditions are near the skip limit.

The maximum values of deceleration (along the flight path) are shown in figure 9. The curves here again appear to cross at one reentry angle. This result can also be attributed to an arbitrary fairing, as described above. Reference 2 presents a method whereby the approximate maximum deceleration may be estimated for steep reentry angles. This method provided data that agreed well with that presented for the steeper entry angles (that is, $\gamma_0 = -15^\circ$ to $\gamma_0 = -20^\circ$) but could not be compared with more shallow entry angles.

Heating Rates

Shown in figure 10 are total convective stagnation-point heat inputs (from $t = 0$ to impact) plotted as a function of the maximum stagnation-point convective heating rate. Convective heating is shown for the range of velocities, reentry angle, and $W/C_D A$ considered.

Note that the data are for a spherical nose having a 1-foot radius. Data for other radii can be found as described in the section "Method" or for other than a sphere by applying appropriate conversions. Figure 11 presents the same type of information except that the radiative

heating has been added. The total stagnation-point heat inputs are plotted as a function of the maximum stagnation-point heating rates. Time histories of the stagnation-point heating rates, with integrated heating indicated, are shown for a variety of initial reentry conditions in figure 12.

Shown in figure 13 are the maximum convective and radiative stagnation-point heat-transfer rates as a function of initial reentry angle for the range of velocity and $W/C_D A$ considered.

L As mentioned, the radiative heat-transfer data of figures 11 and 13
1 are equilibrium values. The theory for this type of heat transfer is
7 fairly well defined. (See ref. 3.) There is some indication (ref. 8,
5 for example) that the radiative heat transfer encountered in reentry
0 may well be nonequilibrium; however, this type of heat transfer is not
well understood at present and is often expressed as a multiple of the
equilibrium value. Therefore, the rates presented can be considered
as a lower limit of the radiative heating.

CONCLUDING REMARKS

Charts have been presented for determination of reentry trajectory information, including heating data, for a wide variety of initial reentry conditions for velocities of 26,000 to 45,000 feet per second. The data are from machine-computed exact solutions of the equations of motion. These charts should be useful in preliminary design of vehicles entering in a ballistic mode. Although they were computed for an initial latitude and azimuth, they may be applied to other combinations of latitude and azimuth angles.

Langley Research Center,
National Aeronautics and Space Administration,
Langley Air Force Base, Va., August 9, 1961.

REFERENCES

1. Chapman, Dean R.: An Analysis of the Corridor and Guidance Requirements for Supercircular Entry Into Planetary Atmospheres. NASA TR R-55, 1960.
2. Allen, H. Julian, and Eggers, A. J., Jr.: A Study of the Motion and Aerodynamic Heating of Ballistic Missiles Entering the Earth's Atmosphere at High Supersonic Speeds. NACA Rep. 1381, 1958. (Supersedes NACA TN 4047.)
3. Perrine, C.: Estimation of Maximum Heating Rates and Total Heat Load During Supercircular Re-entry. MLV TN-10, The Martin Co., Aug. 1960.
4. Nielsen, Jack N., Goodwin, Frederick K., and Mersman, William A.: Three-Dimensional Orbits of Earth Satellites, Including Effects of Earth Oblateness and Atmospheric Rotation. NASA MEMO 12-4-58A, 1958.
5. Herrick, Samuel, and Walters, Louis G.: The Influence of the Earth's Potential Field on a Nearly Circular Satellite. Pub. No. U-326, Aeronutronic (Newport Beach, Calif.), Jan. 9, 1959.
6. Minzner, R. A., Champion, K. S. W., and Pond, H. L.: The ARDC Model Atmosphere, 1959. Air Force Surveys in Geophysics No. 115 (AFCRC-TR-59-267), Air Force Cambridge Res. Center, Aug. 1959.
7. Chapman, Dean R.: An Approximate Analytical Method for Studying Entry Into Planetary Atmospheres. NASA TR R-11, 1959. (Supersedes NACA TN 4276.)
8. Kivel, Bennett: Radiation From Hot Air and Stagnation Heating. Res. Rep. 79 (AFBMD-TR-59-20), Avco-Everett Res. Lab., Oct. 1959.

L
1
7
5
0

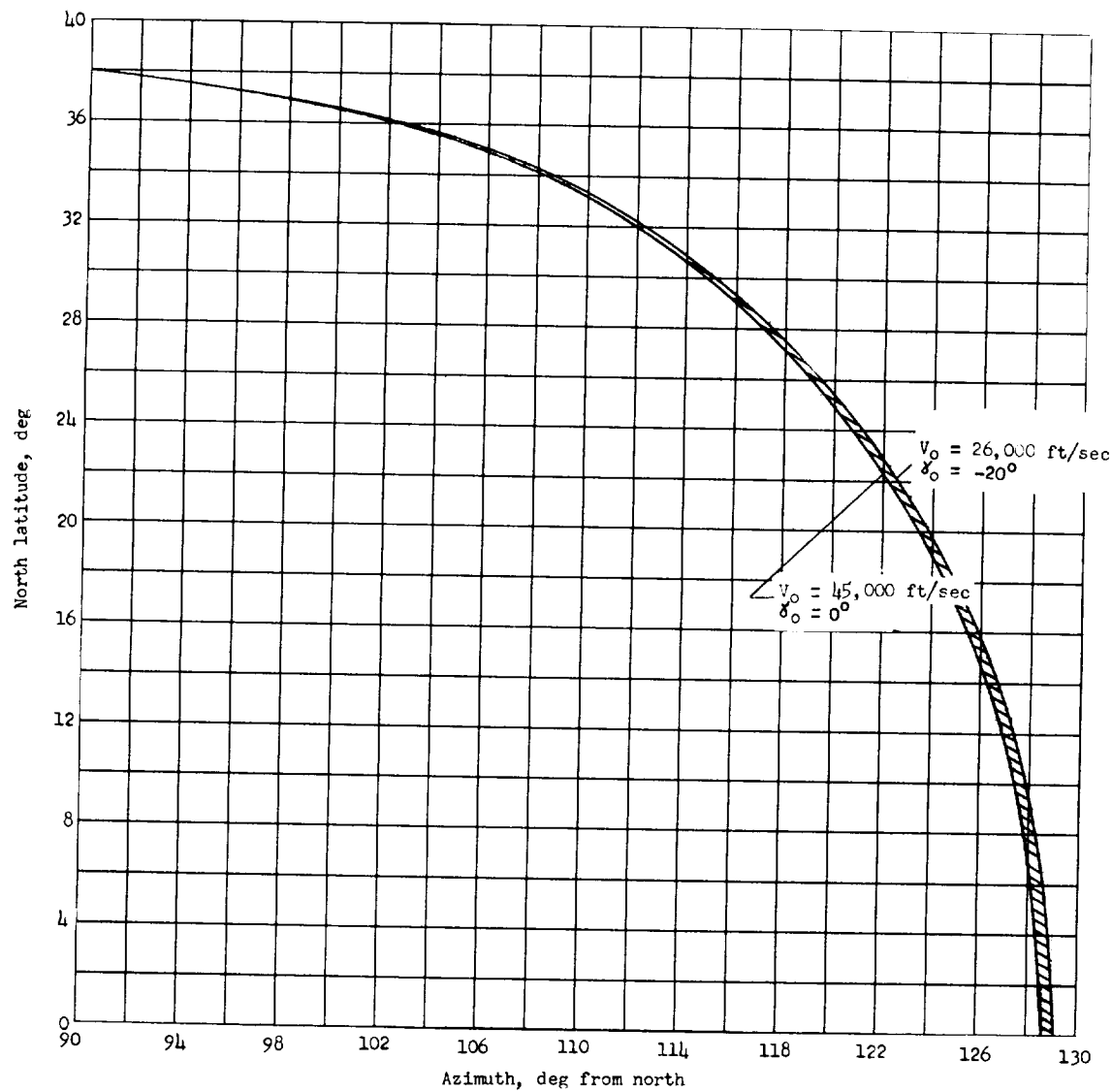


Figure 1.- Azimuth corrections for varying latitudes.

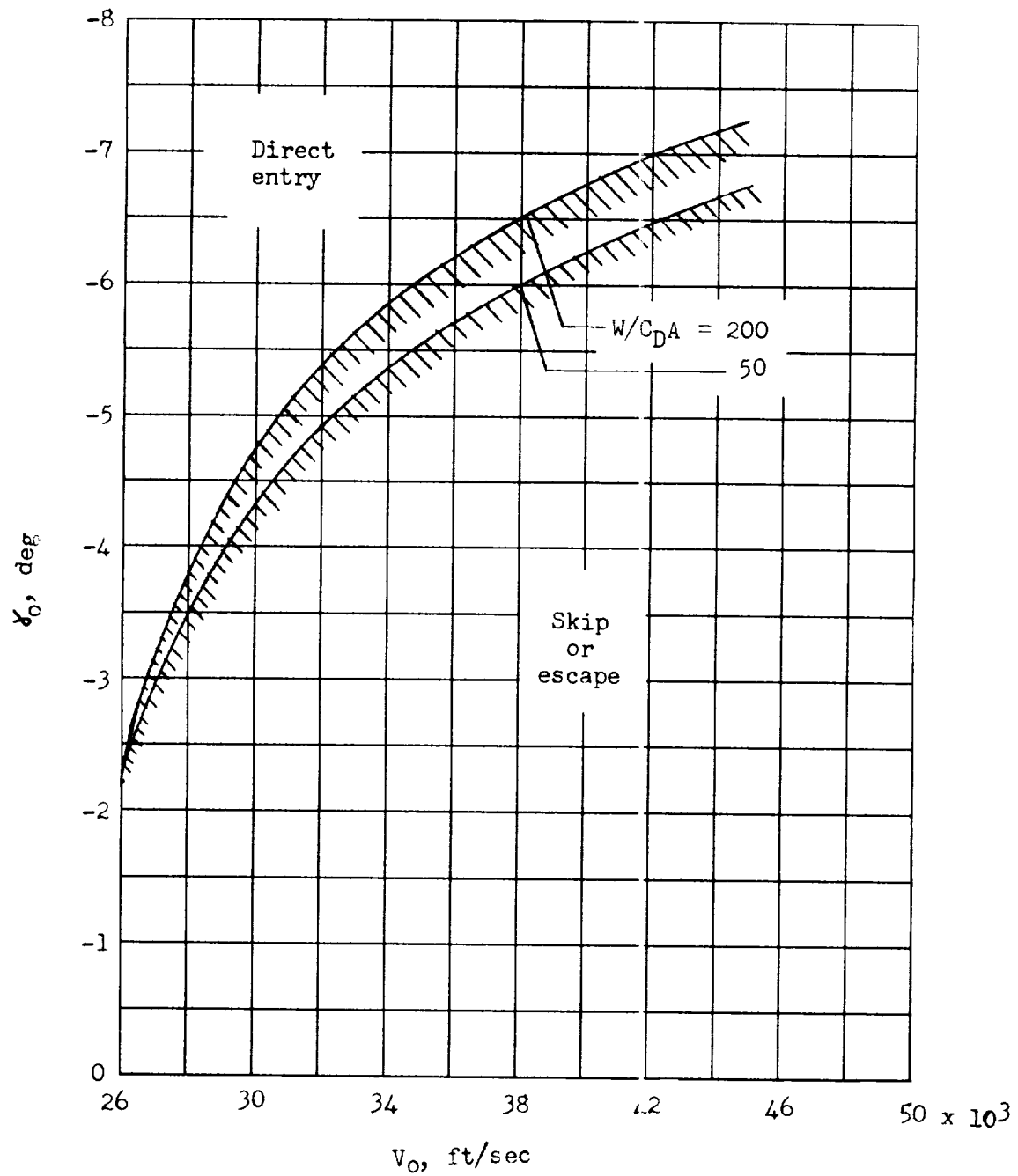
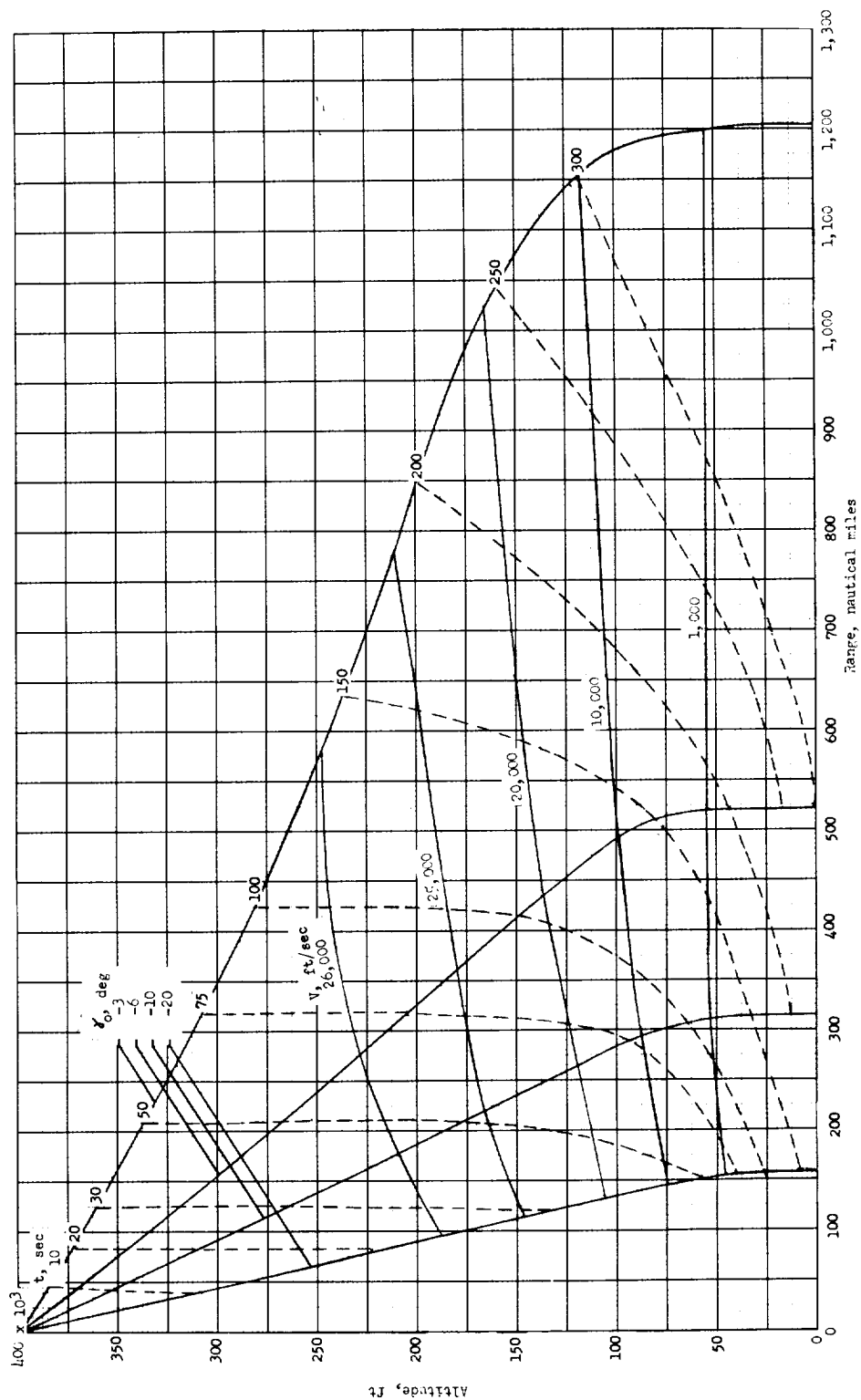
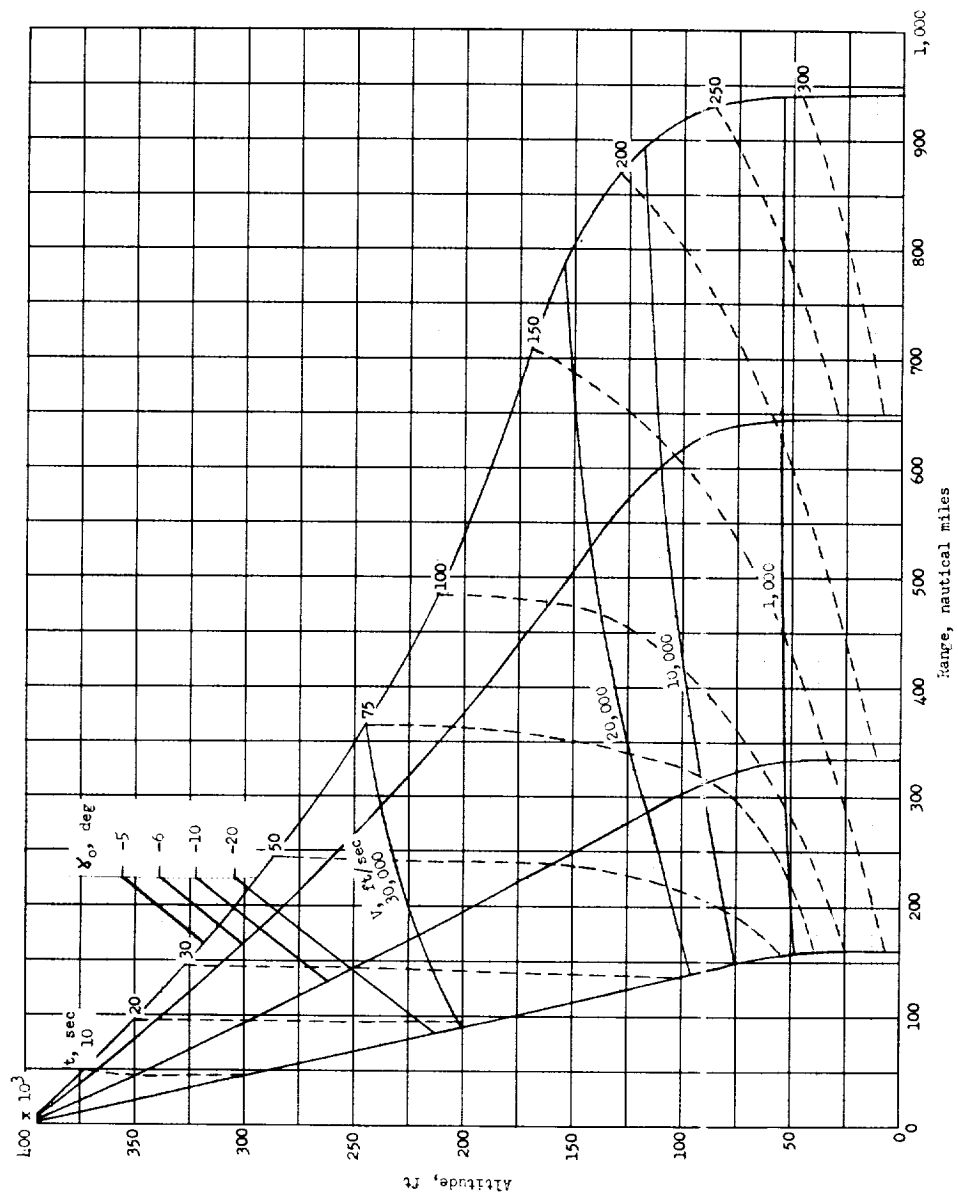


Figure 2.- Skip limits. $h_0 = 400,000$ feet; accuracy = $\pm 0.25^\circ$.



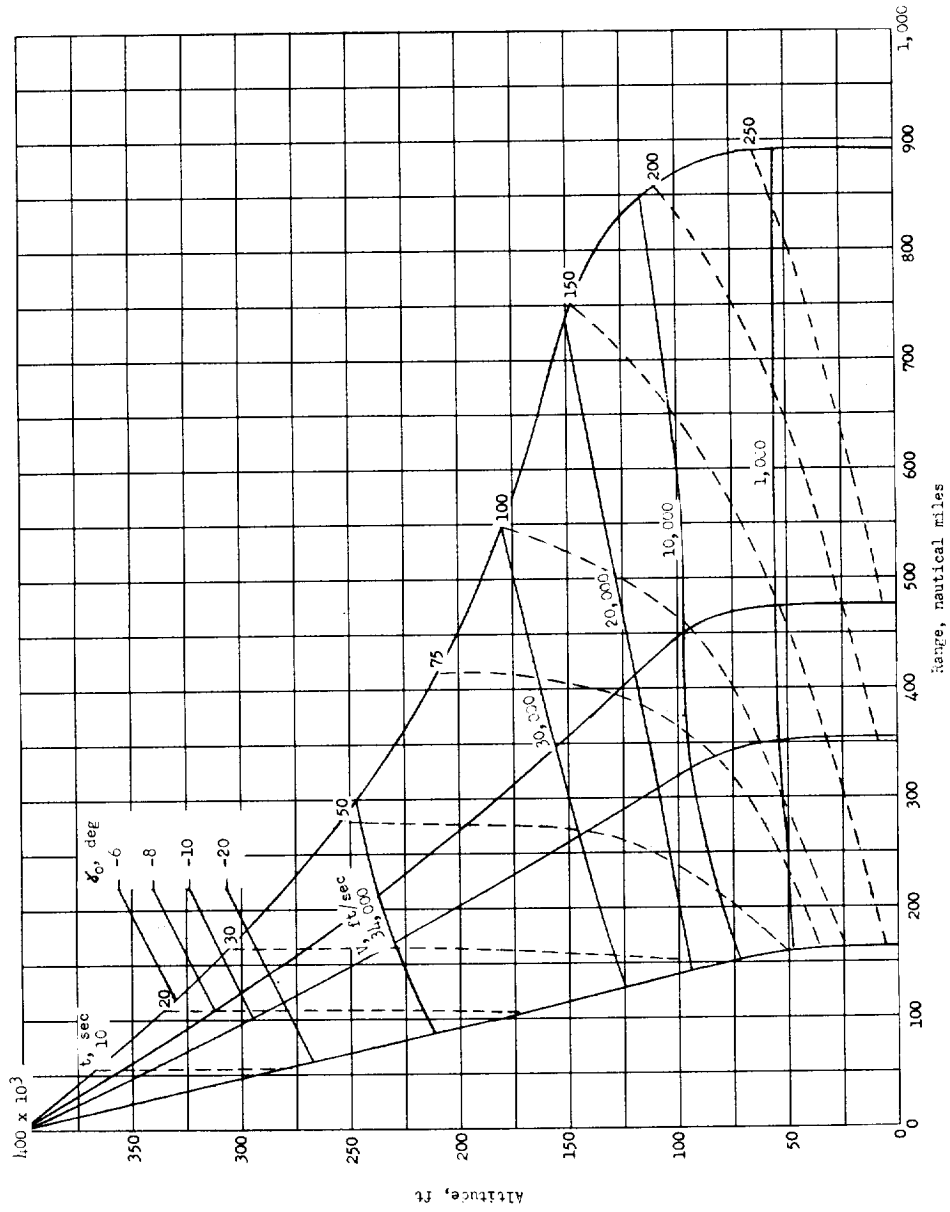
(a) $V_0 = 26,000$ feet per second.

Figure 3.- Altitude-range profile. $\frac{W}{C_{DA}} = 100$.



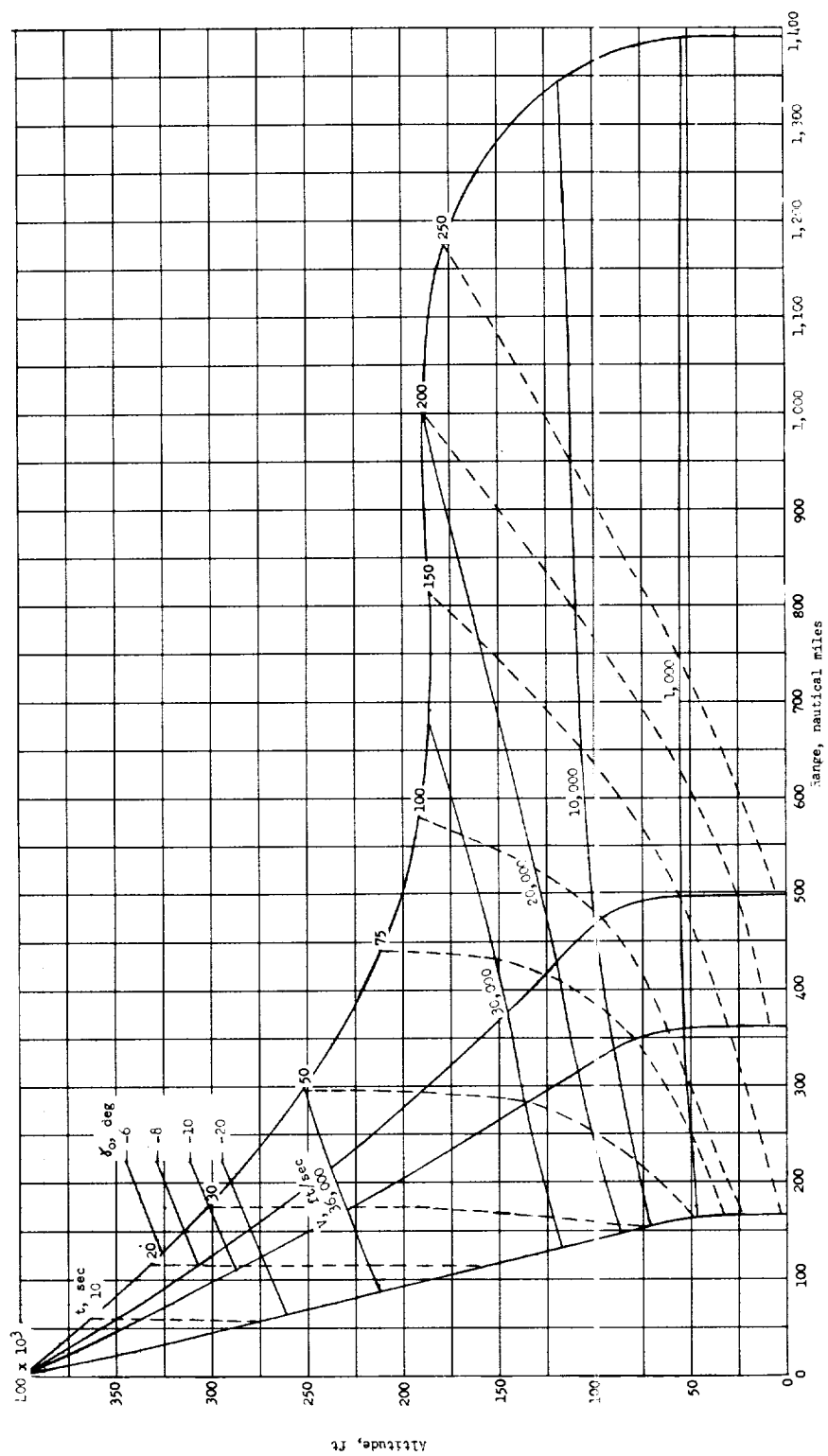
(b) $V_0 = 30,000$ feet per second.

Figure 3.- Continued.



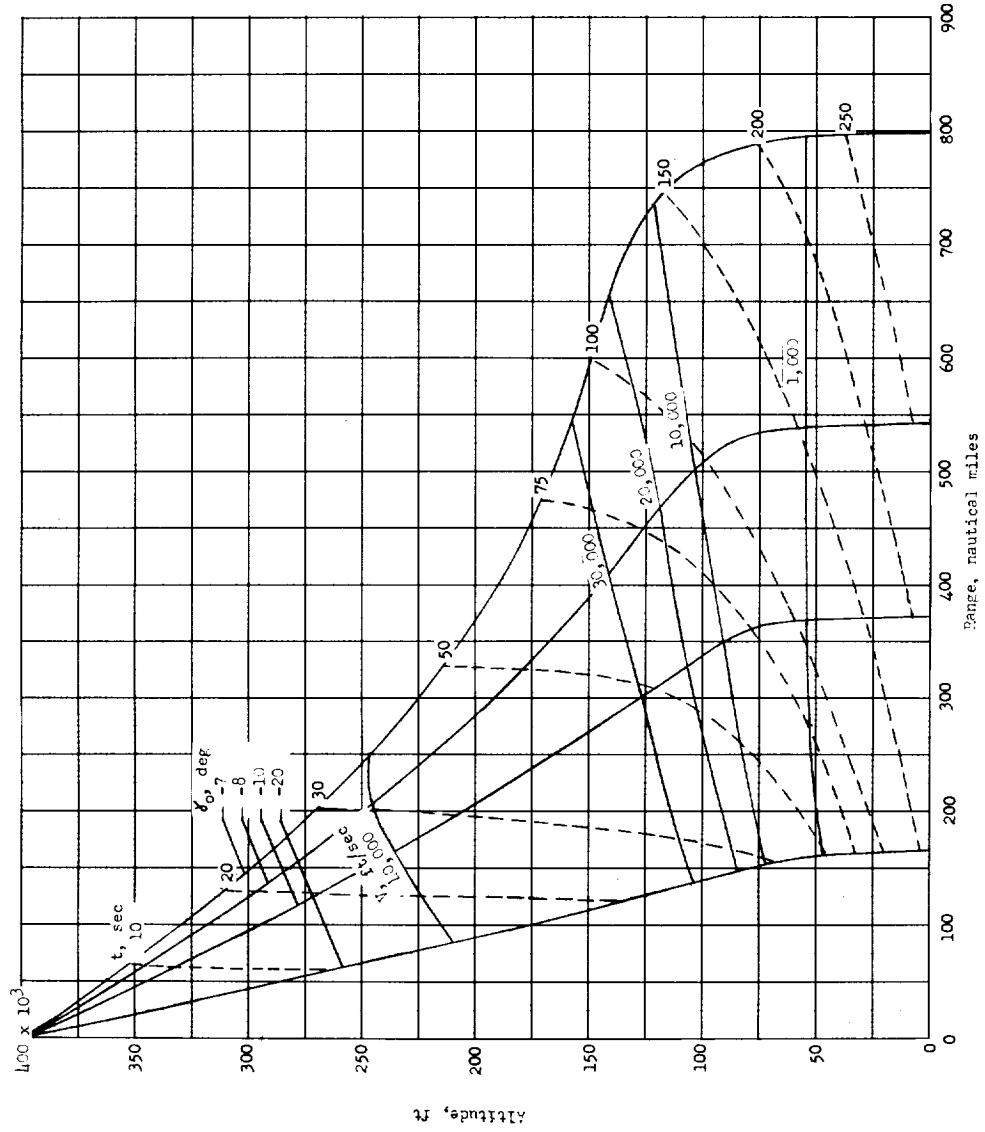
(c) $V_0 = 34,000$ feet per second.

Figure 3.- Continued.



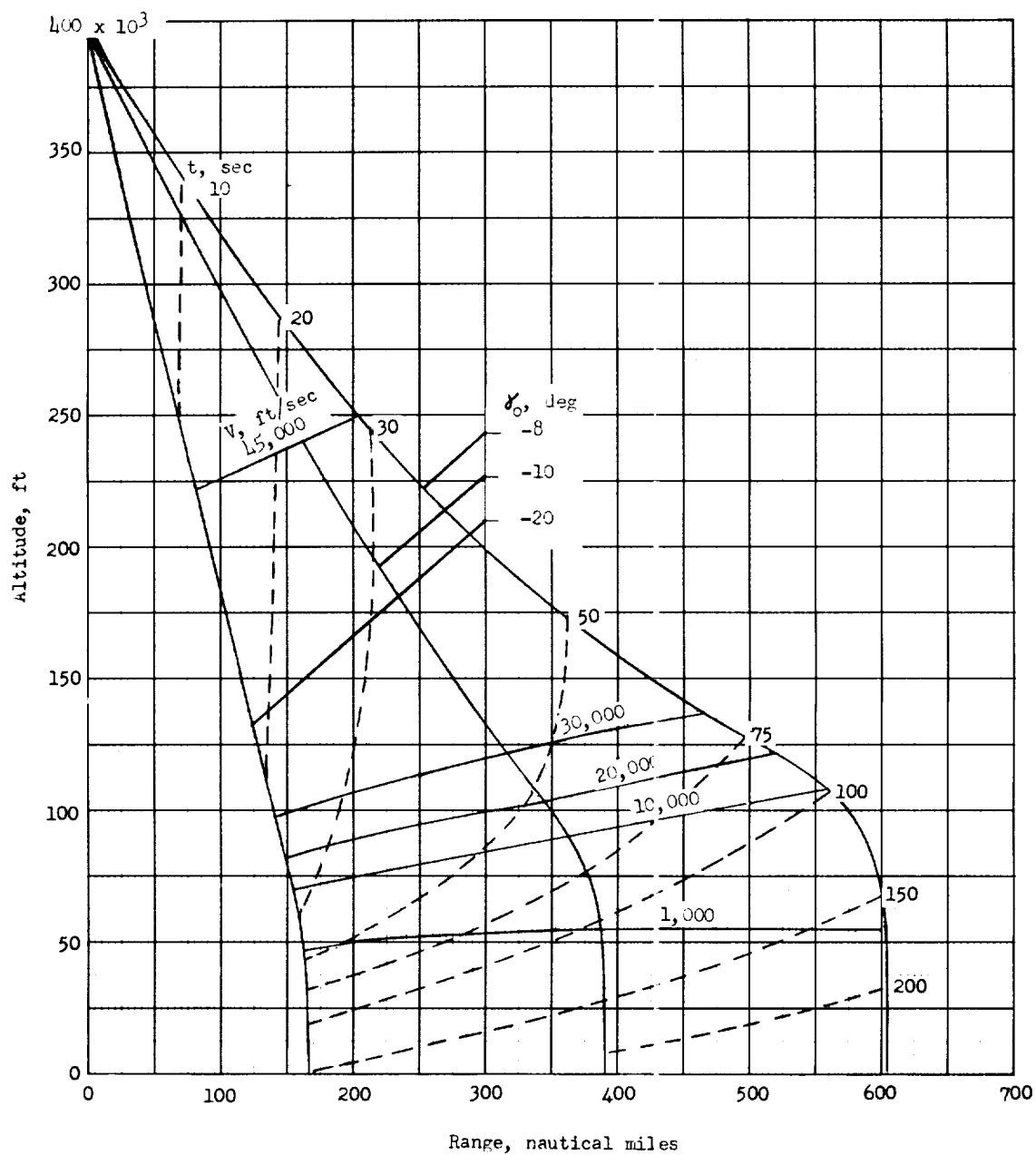
(d) $V_0 = 36,000$ feet per second.

Figure 3.- Continued.



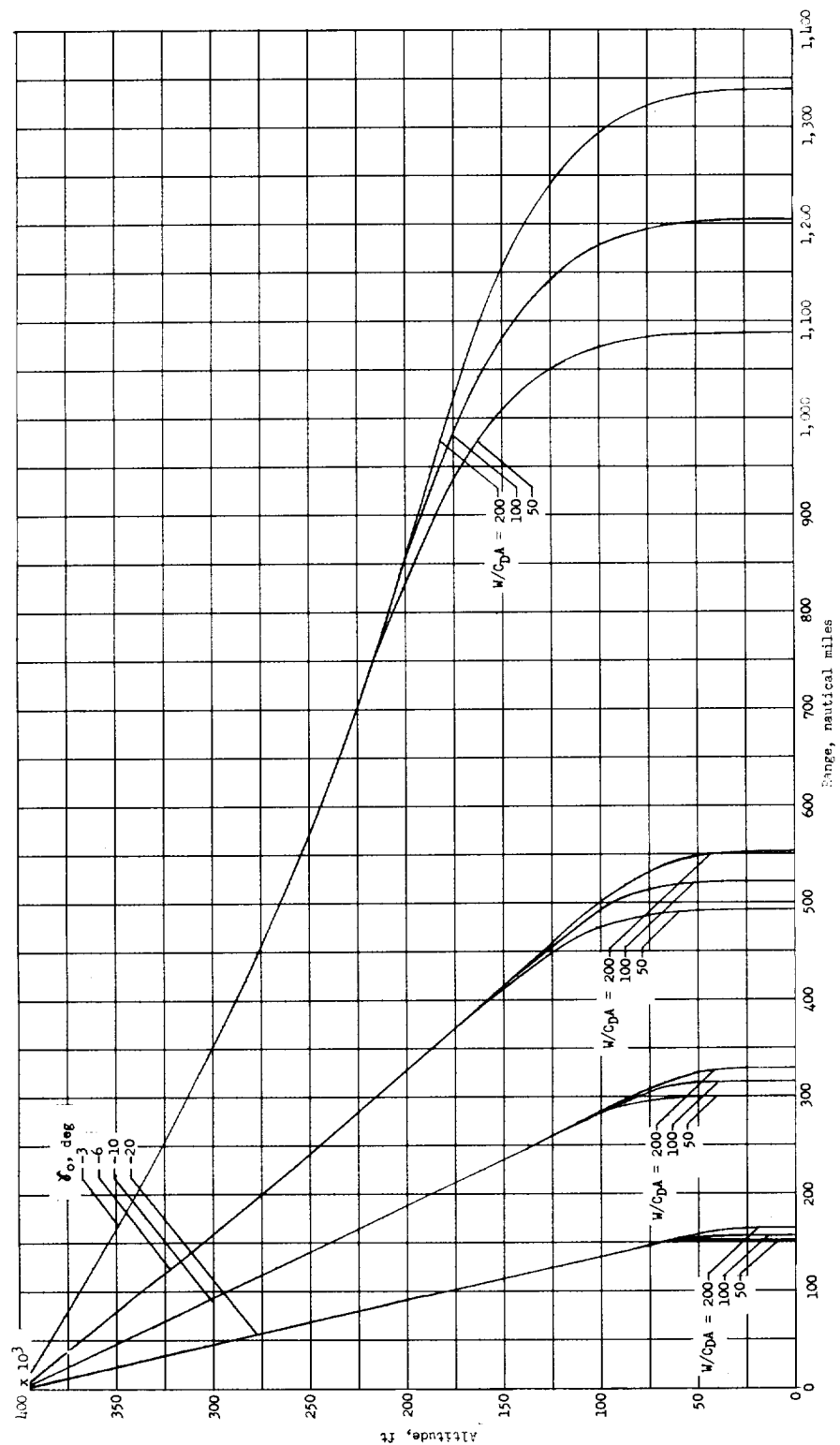
(e) $V_0 = 40,000$ feet per second.

Figure 3.- Continued.



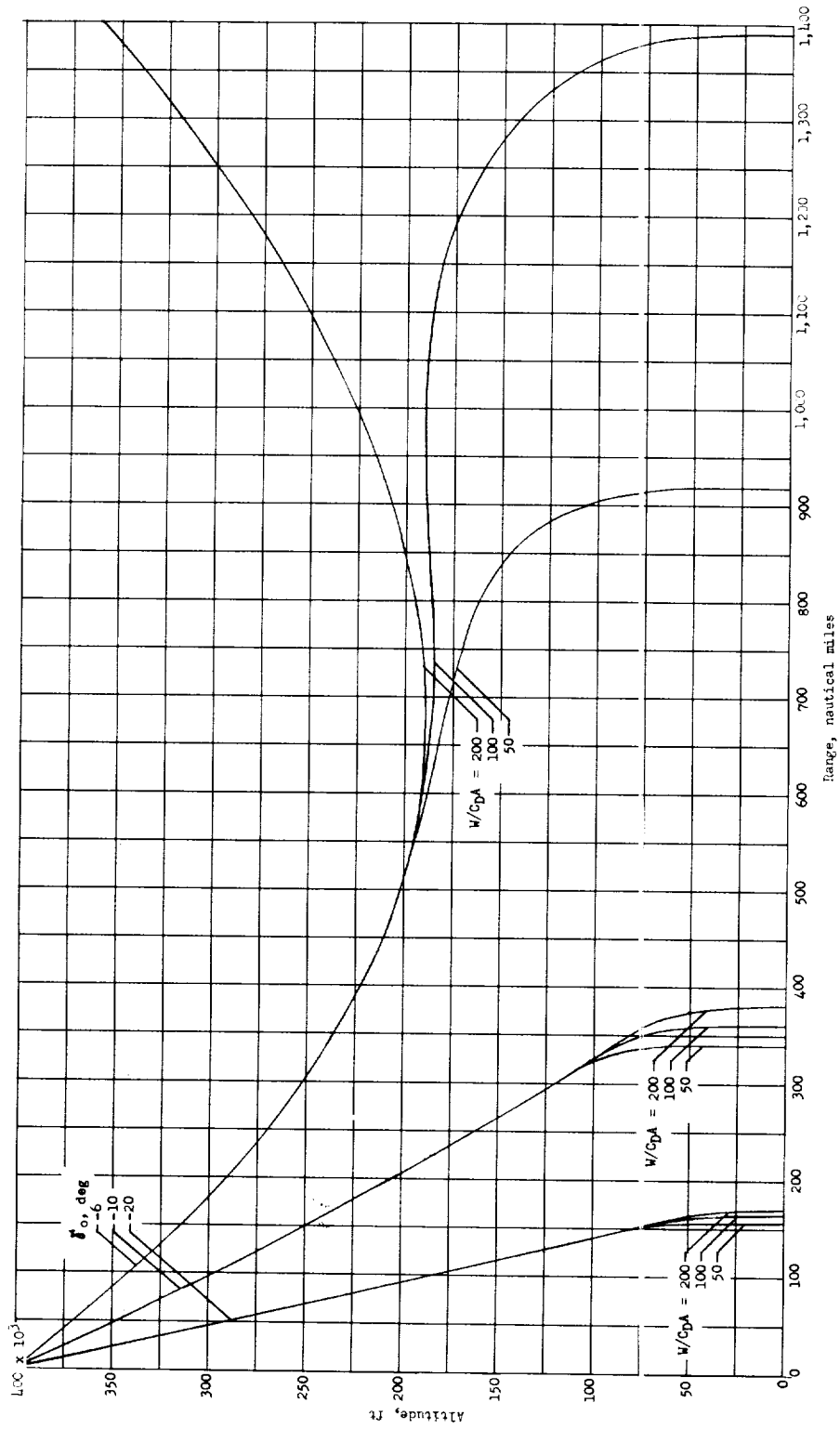
(f) $V_0 = 45,000$ feet per second.

Figure 3.- Concluded.



(a) $V_0 = 26,000$ feet per second.

Figure 4.- Altitude-range profile.



(b) $V_0 = 36,000$ feet per second.

Figure 4.- Continued.

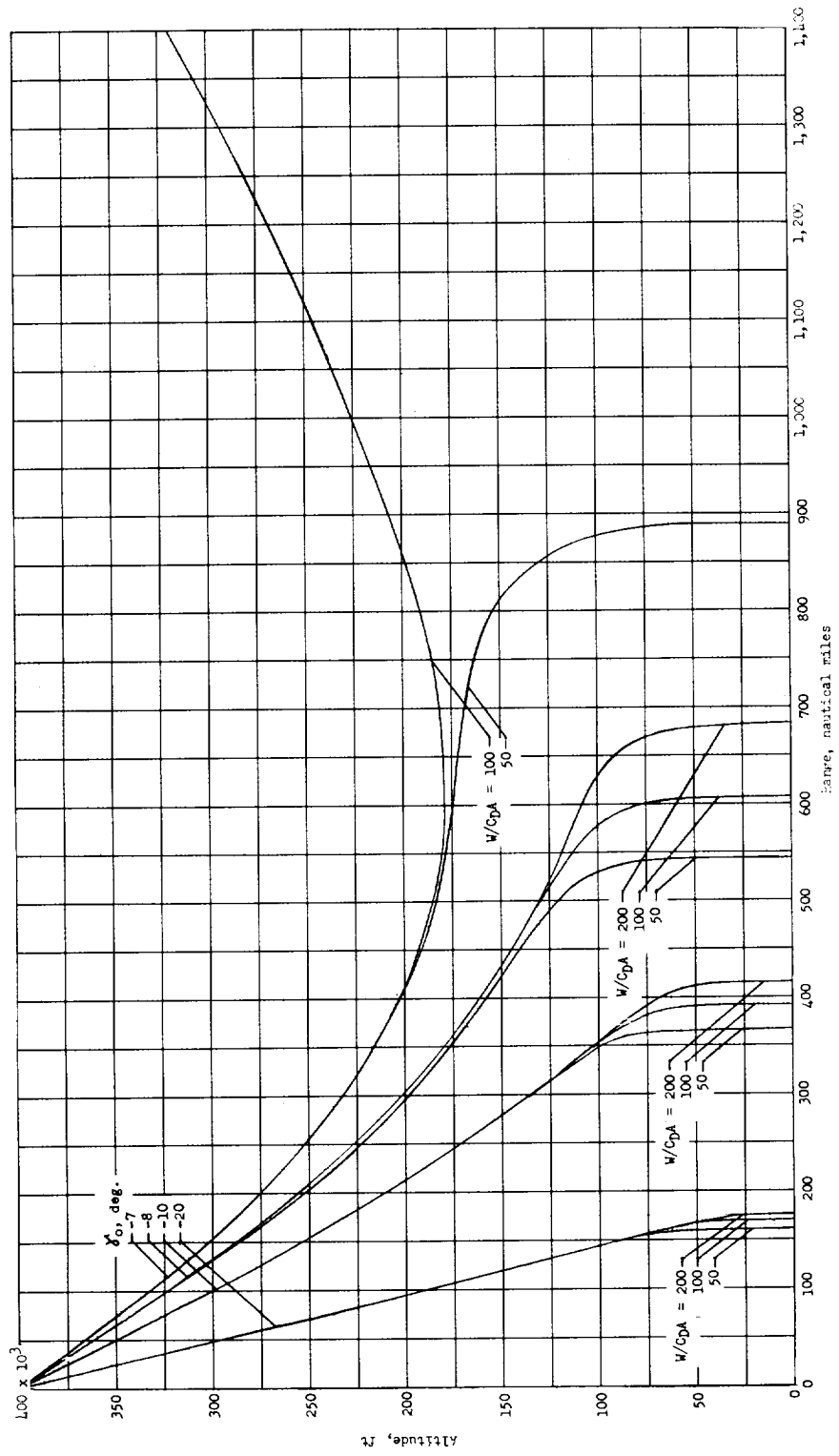
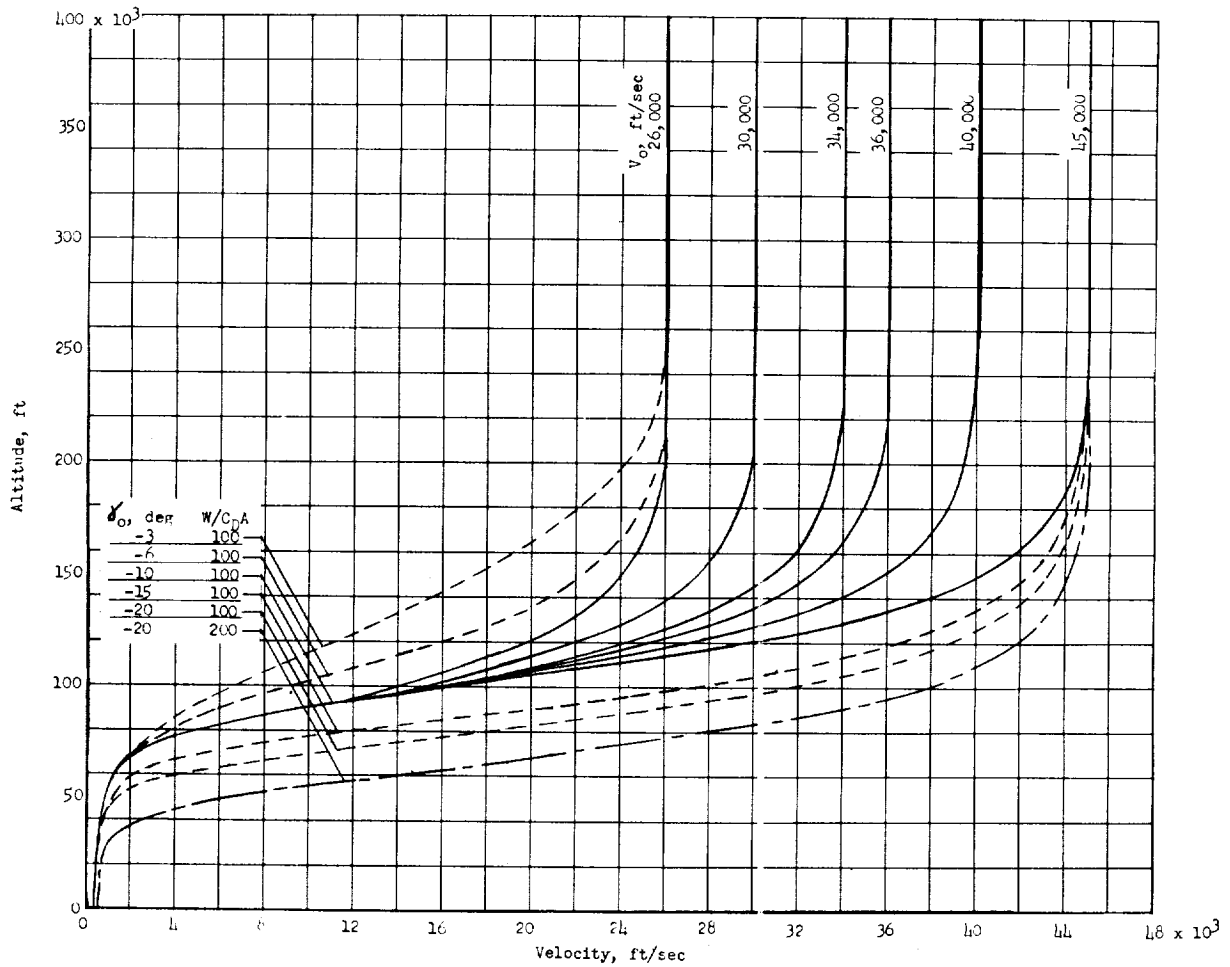
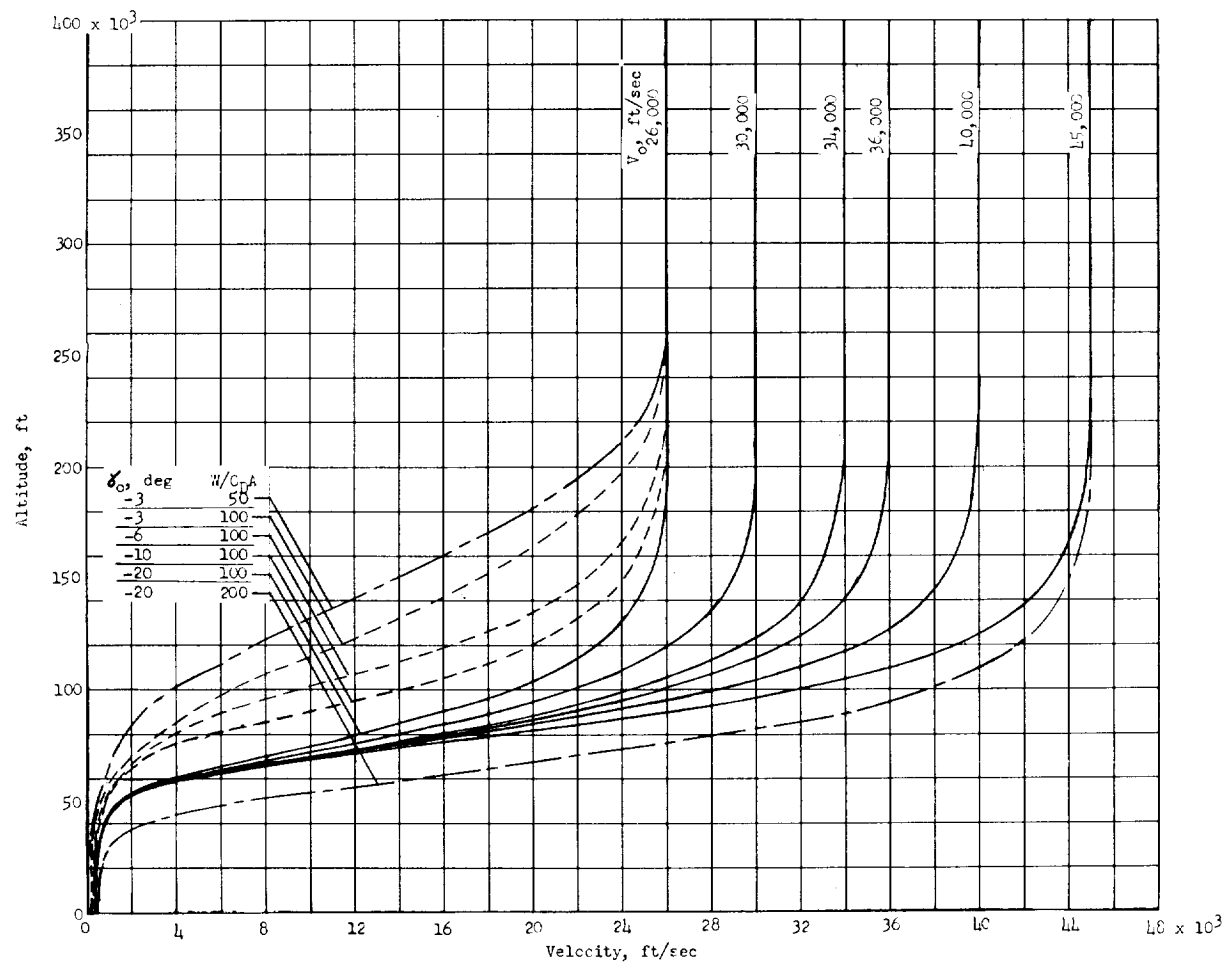
(c) $V_0 = 45,000$ feet per second.

Figure 4.- Concluded.



(a) $\gamma_0 = -10^\circ$.

Figure 5.- Altitude-velocity profile for $\frac{W}{C_D A} = 100$.



(b) $\gamma_0 = -20^\circ$.

Figure 5.- Concluded.

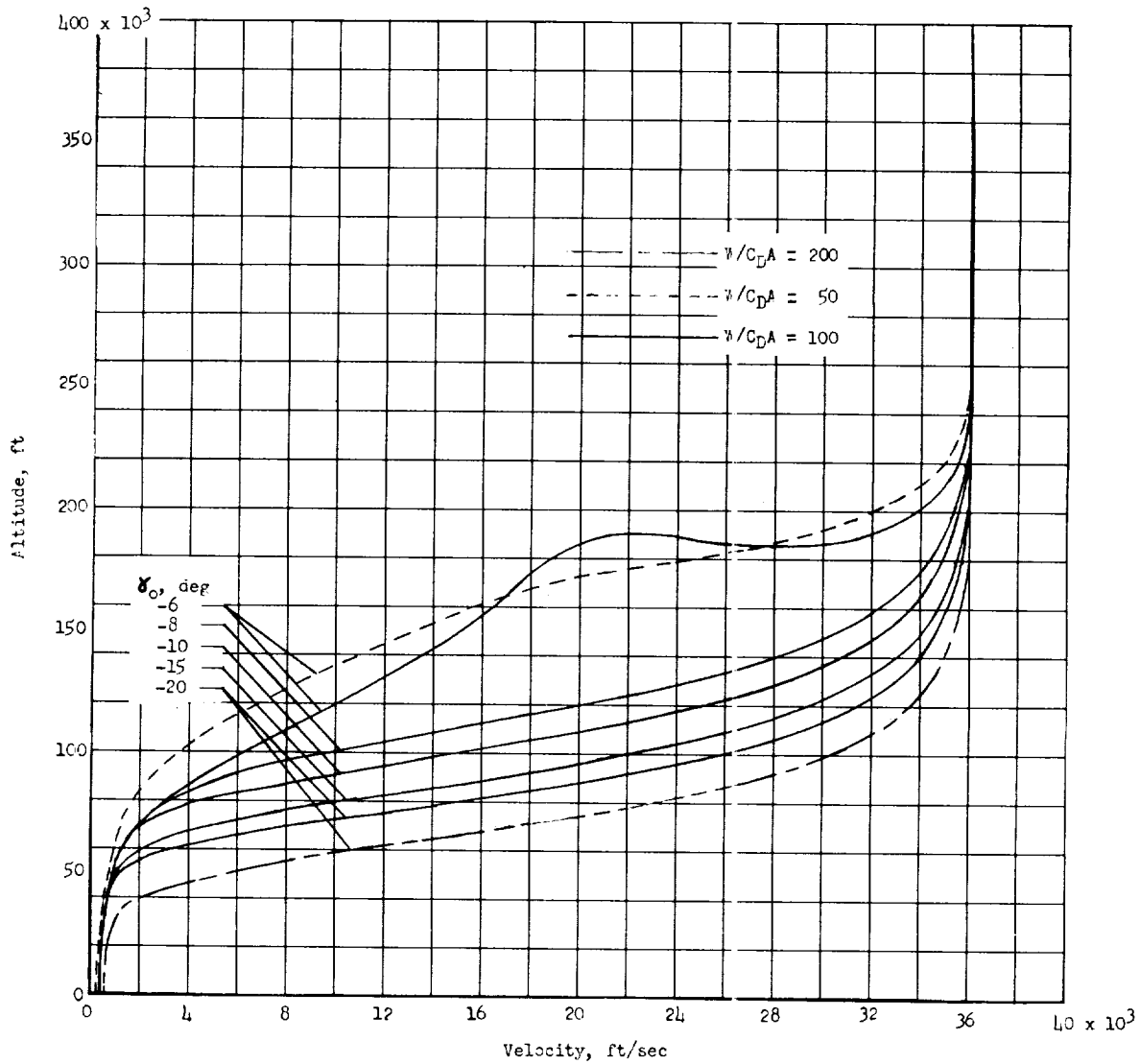
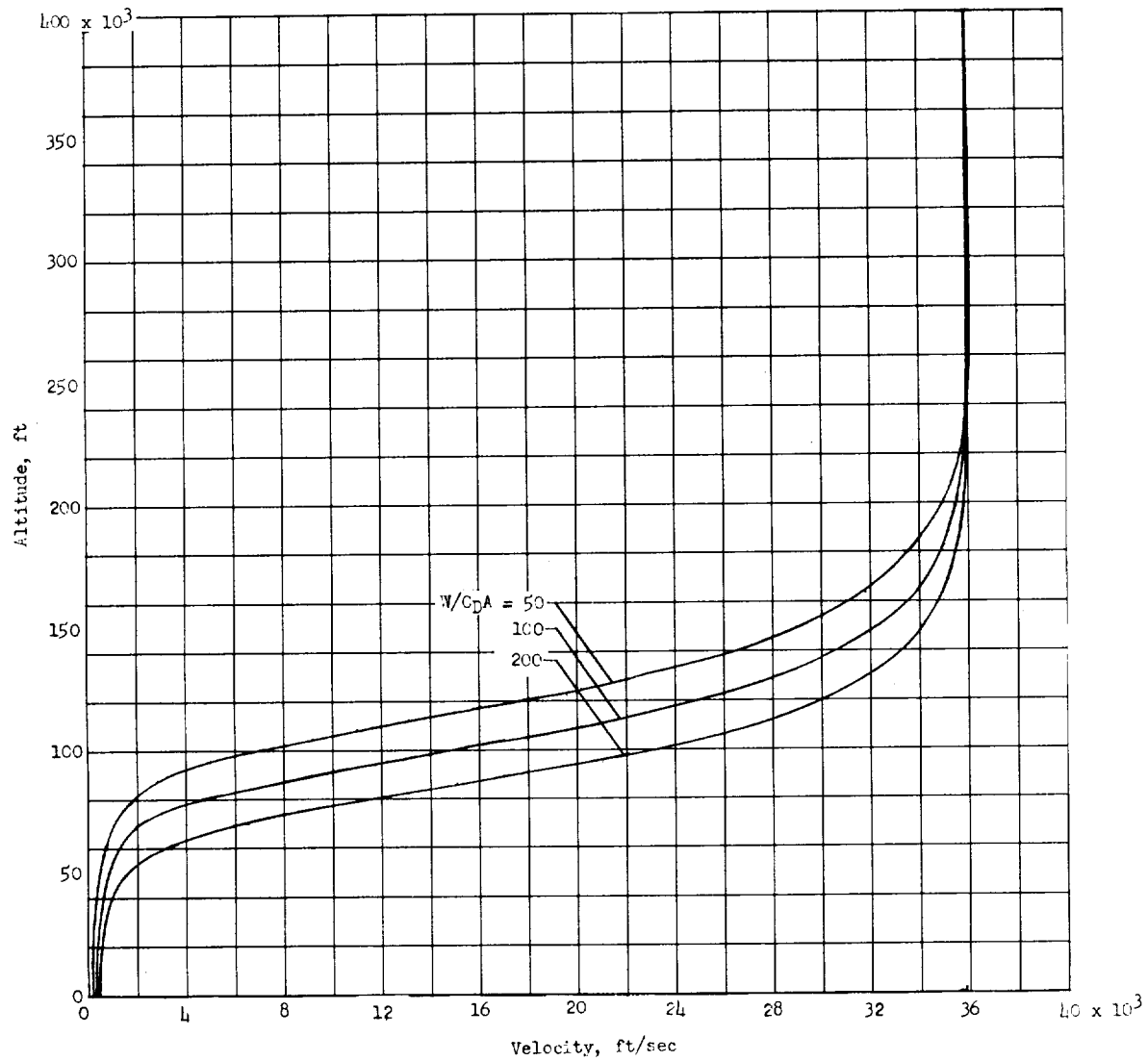
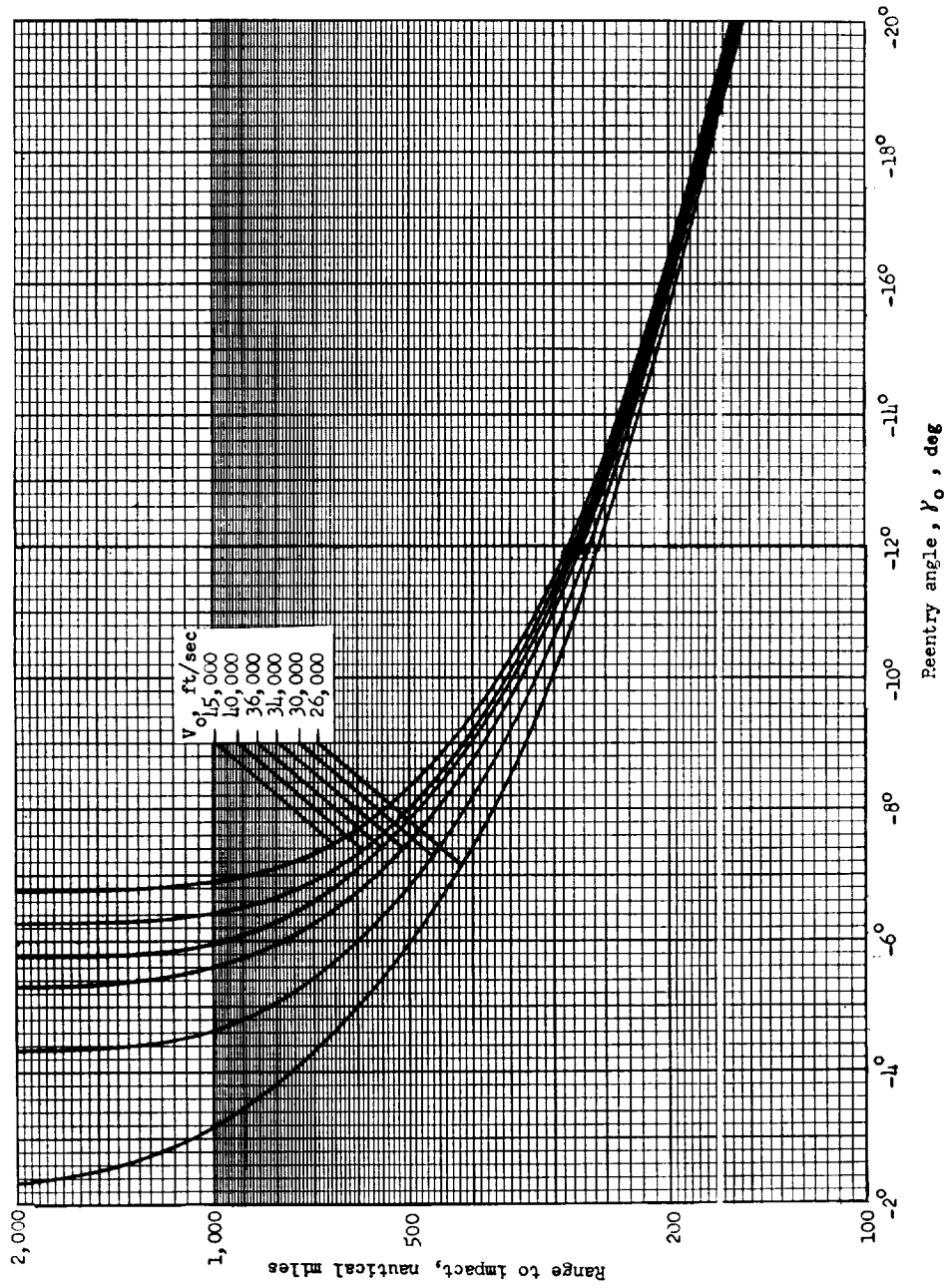
(a) Effects of γ_0 .

Figure 6.- Altitude-velocity profile for $V_0 = 36,000$ feet per second.



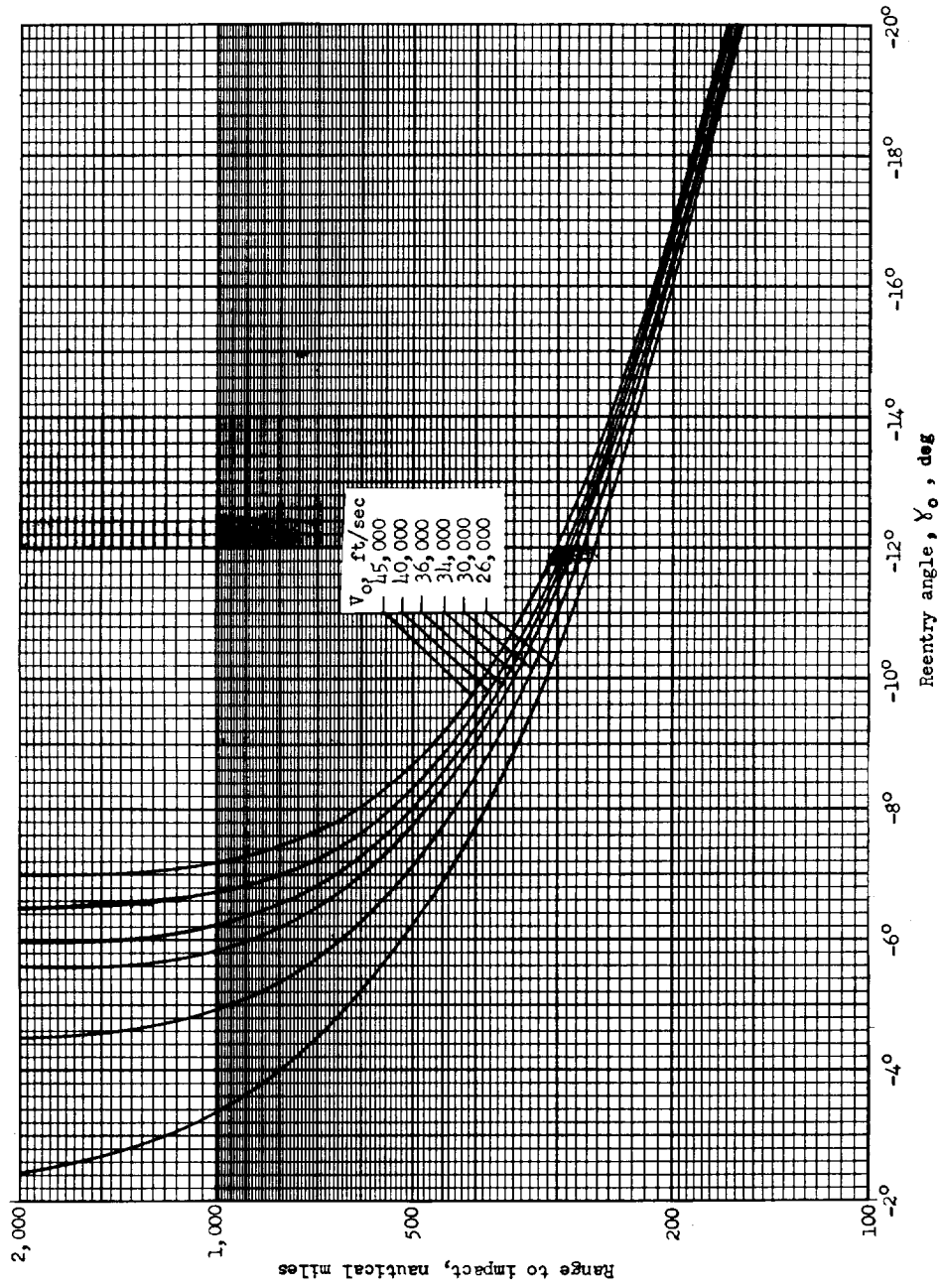
(b) $\frac{W}{C_{DA}}$ effects; $V_0 = 36,000$ feet per second; $\gamma_0 = -10^\circ$.

Figure 6.- Concluded.



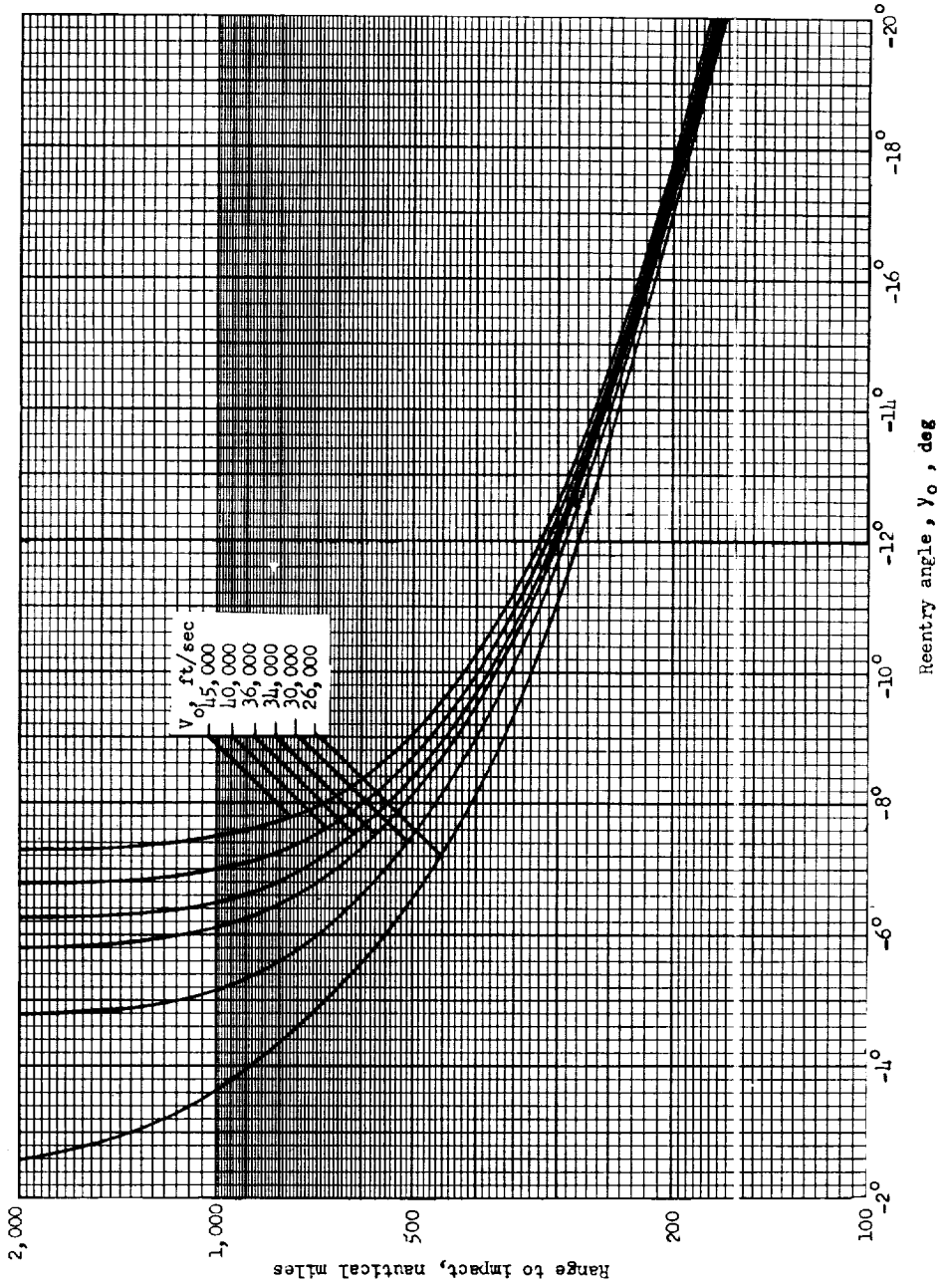
(a) $\frac{W}{C_{DA}} = 50$.

Figure 7.- Range to impact.



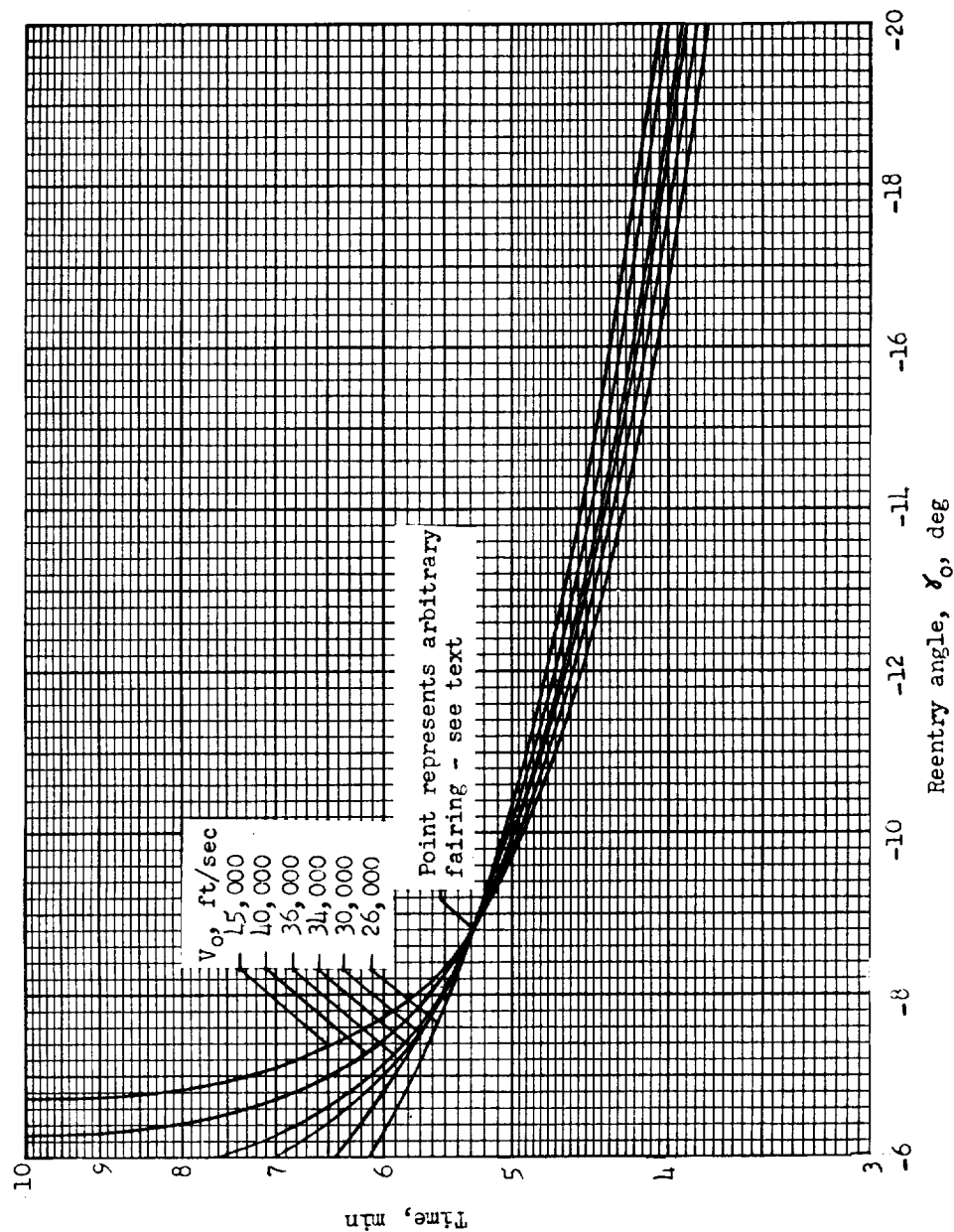
(b) $\frac{W}{C_{DA}} = 100.$

Figure 7.- Continued.



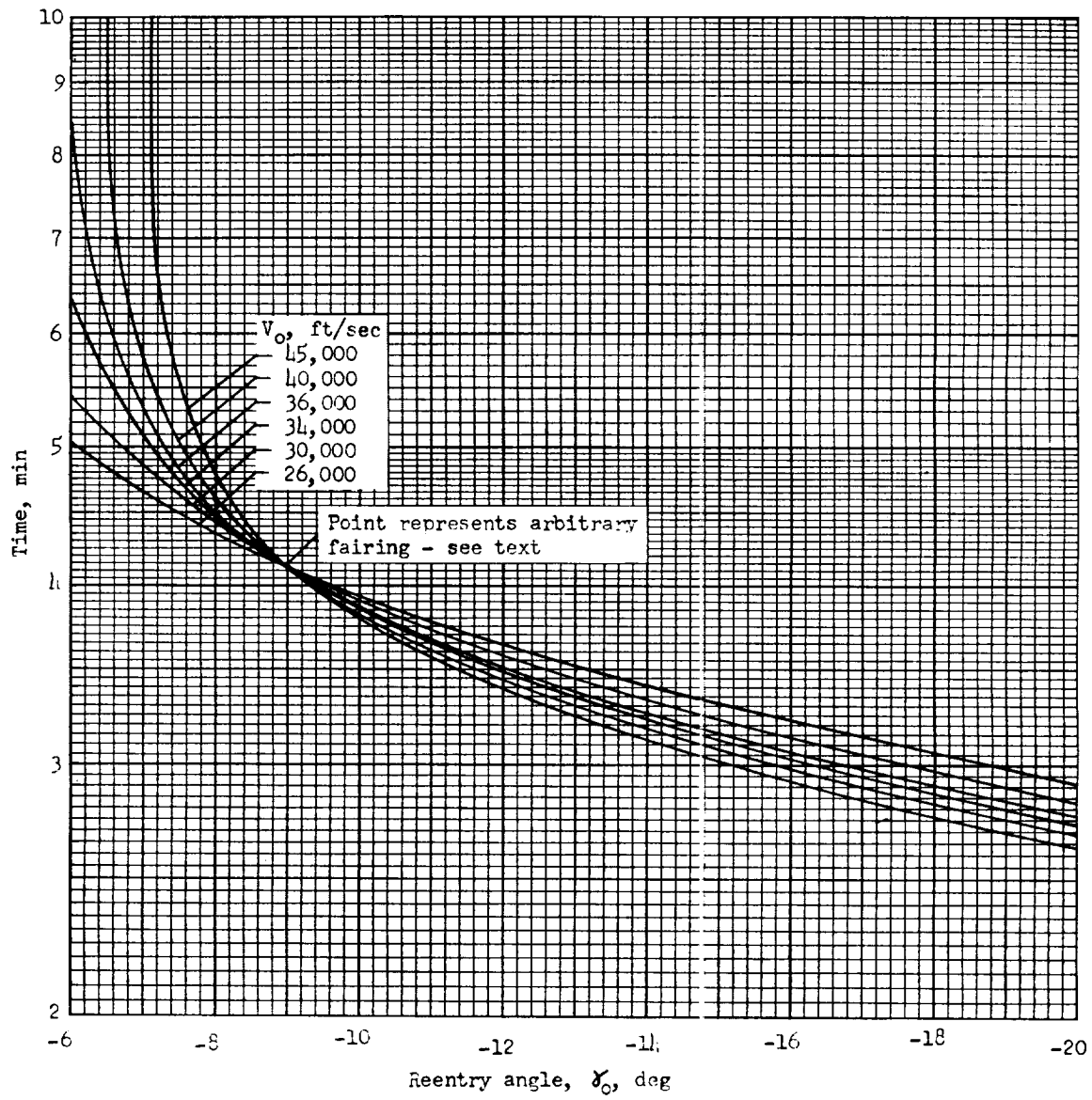
(c) $\frac{W}{C_{DA}} = 200$.

Figure 7.- Concluded.



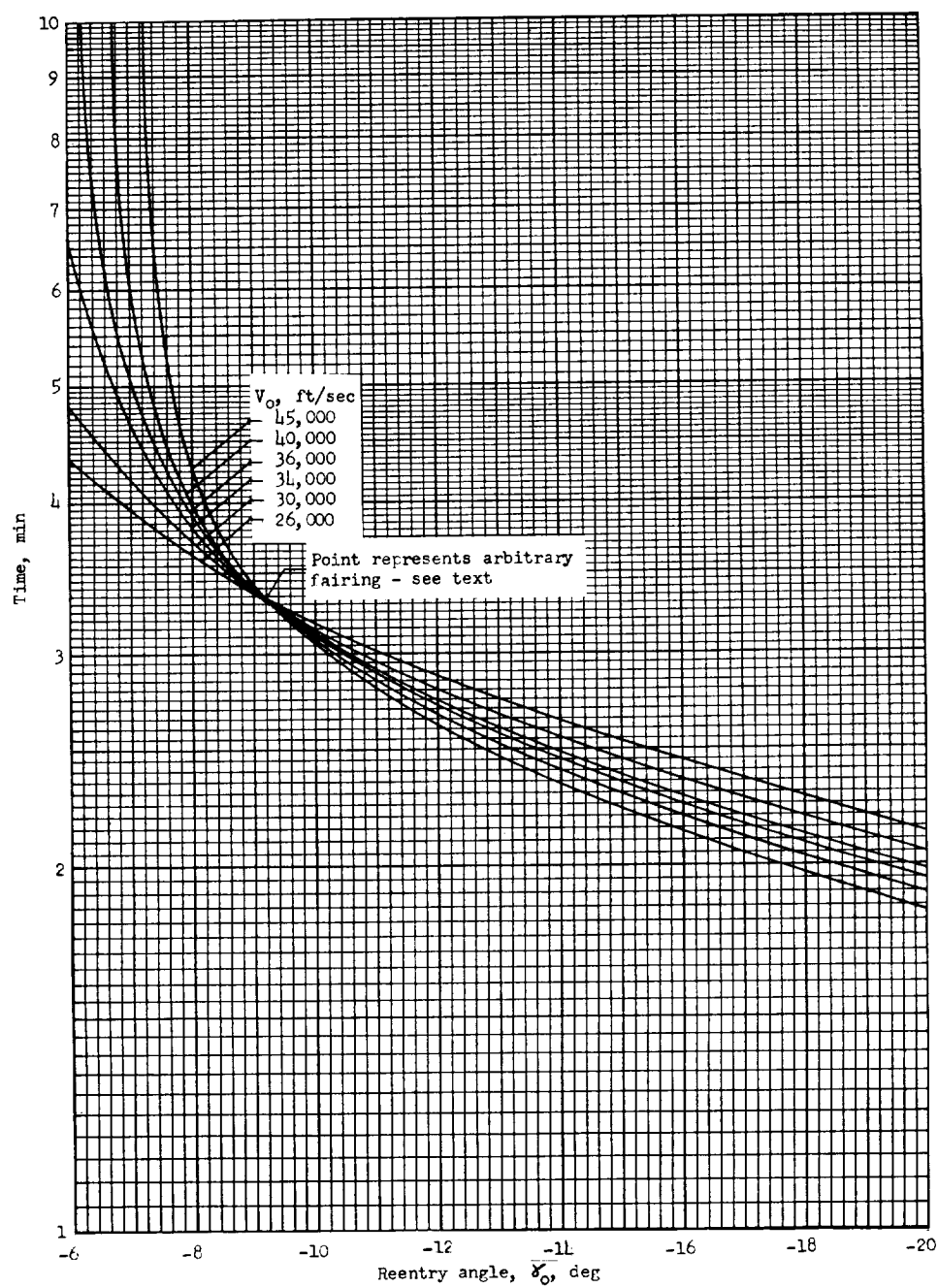
$$(a) \frac{W}{C_D A} = 50.$$

Figure 8.- Time to slow to a speed of 10,000 feet per second.



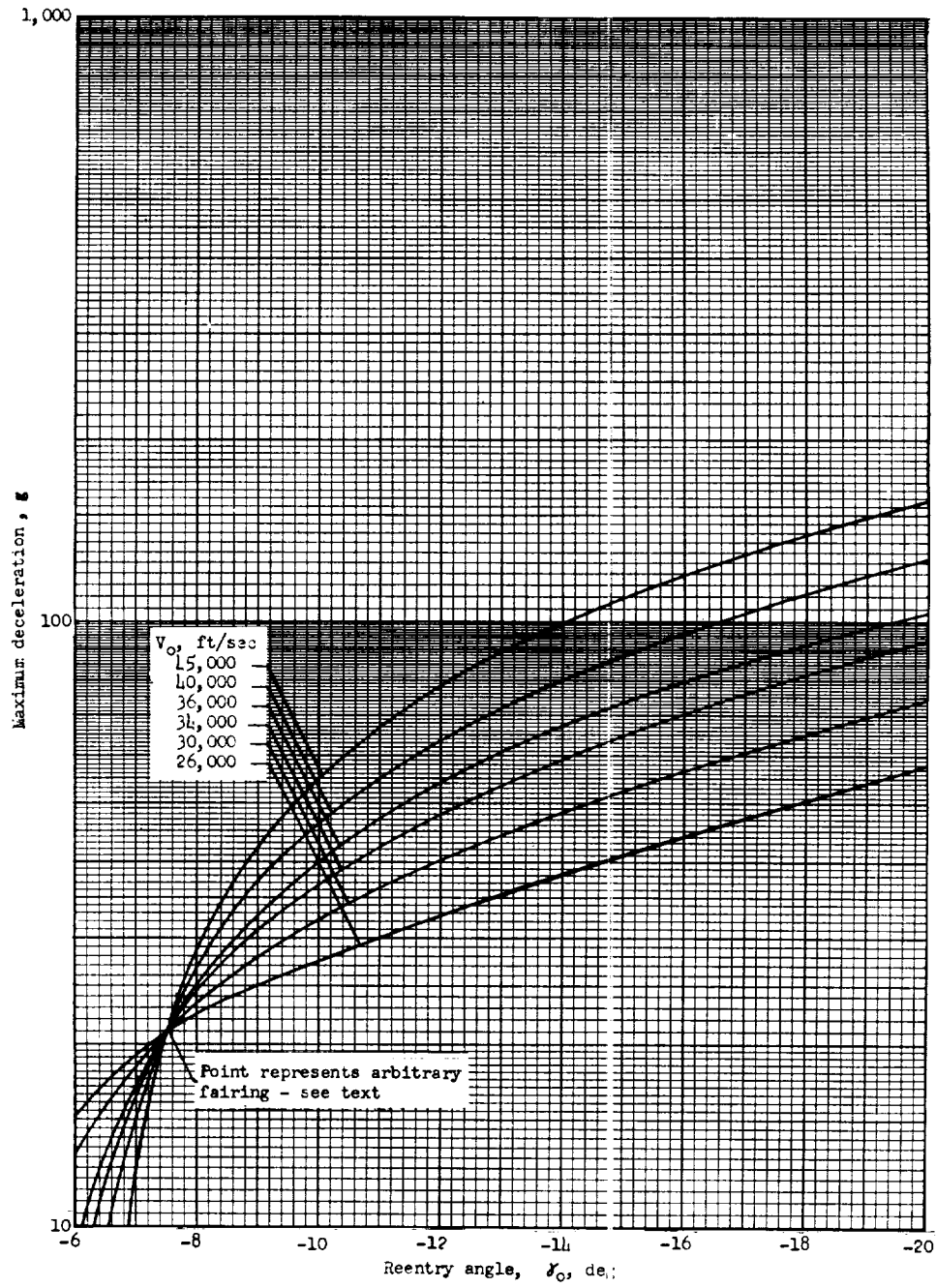
(b) $\frac{W}{C_D A} = 100.$

Figure 8.- Continued.



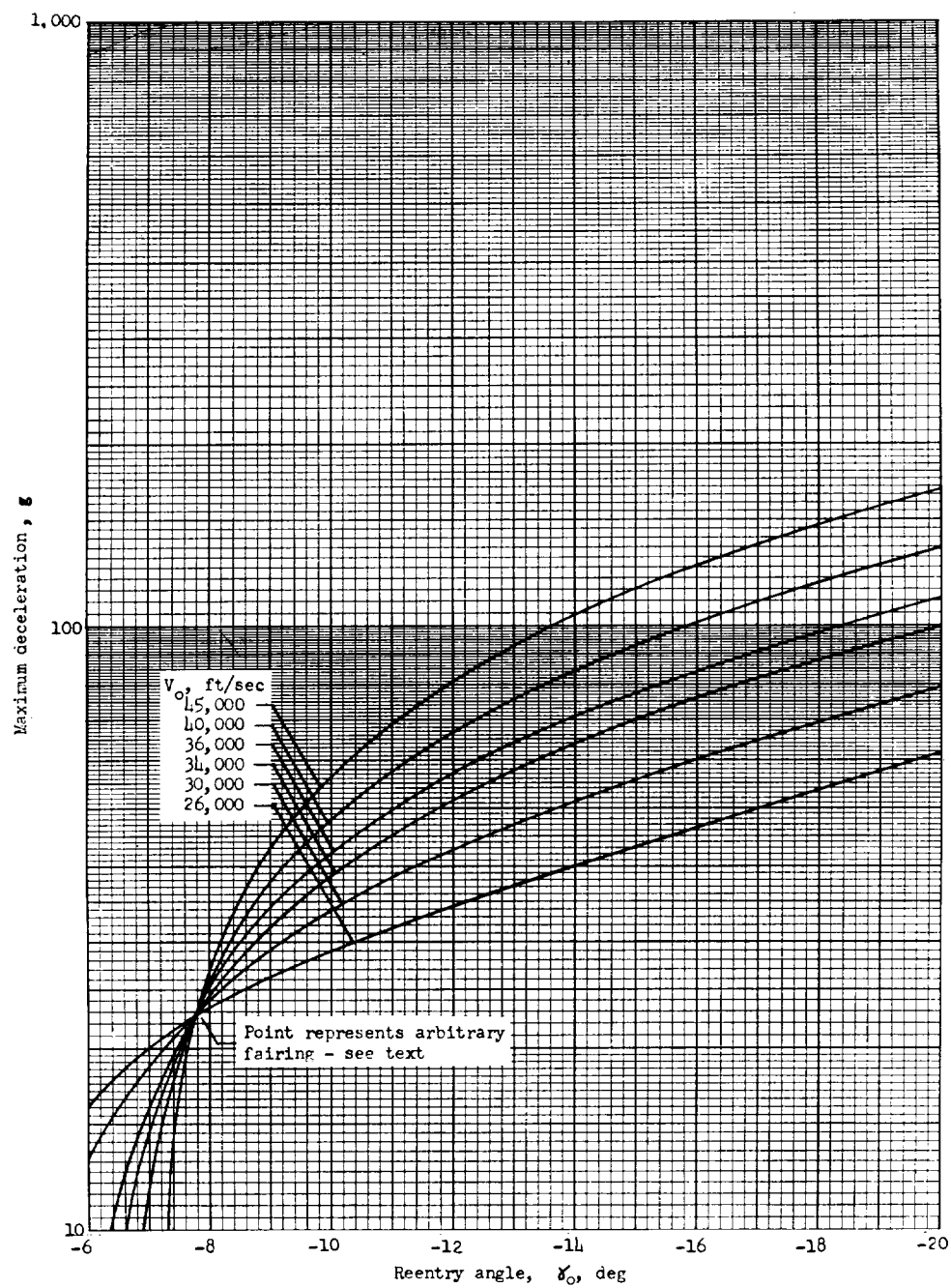
$$(c) \quad \frac{W}{C_D A} = 200.$$

Figure 8.- Concluded.



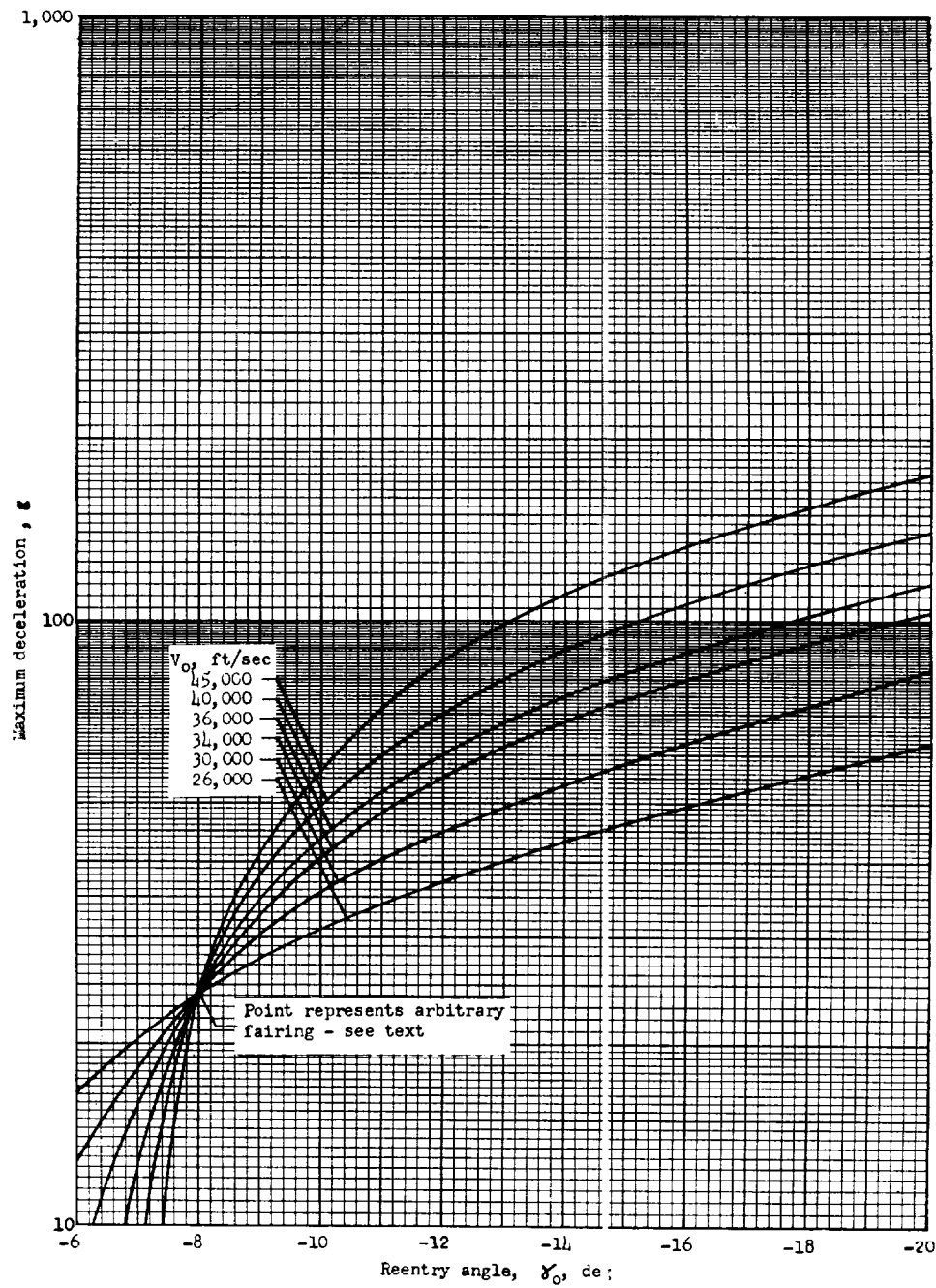
$$(a) \frac{W}{C_D A} = 50.$$

Figure 9.- Deceleration.



(b) $\frac{W}{C_D A} = 100.$

Figure 9.- Continued.



$$(c) \frac{W}{C_D A} = 200.$$

Figure 9.- Concluded.

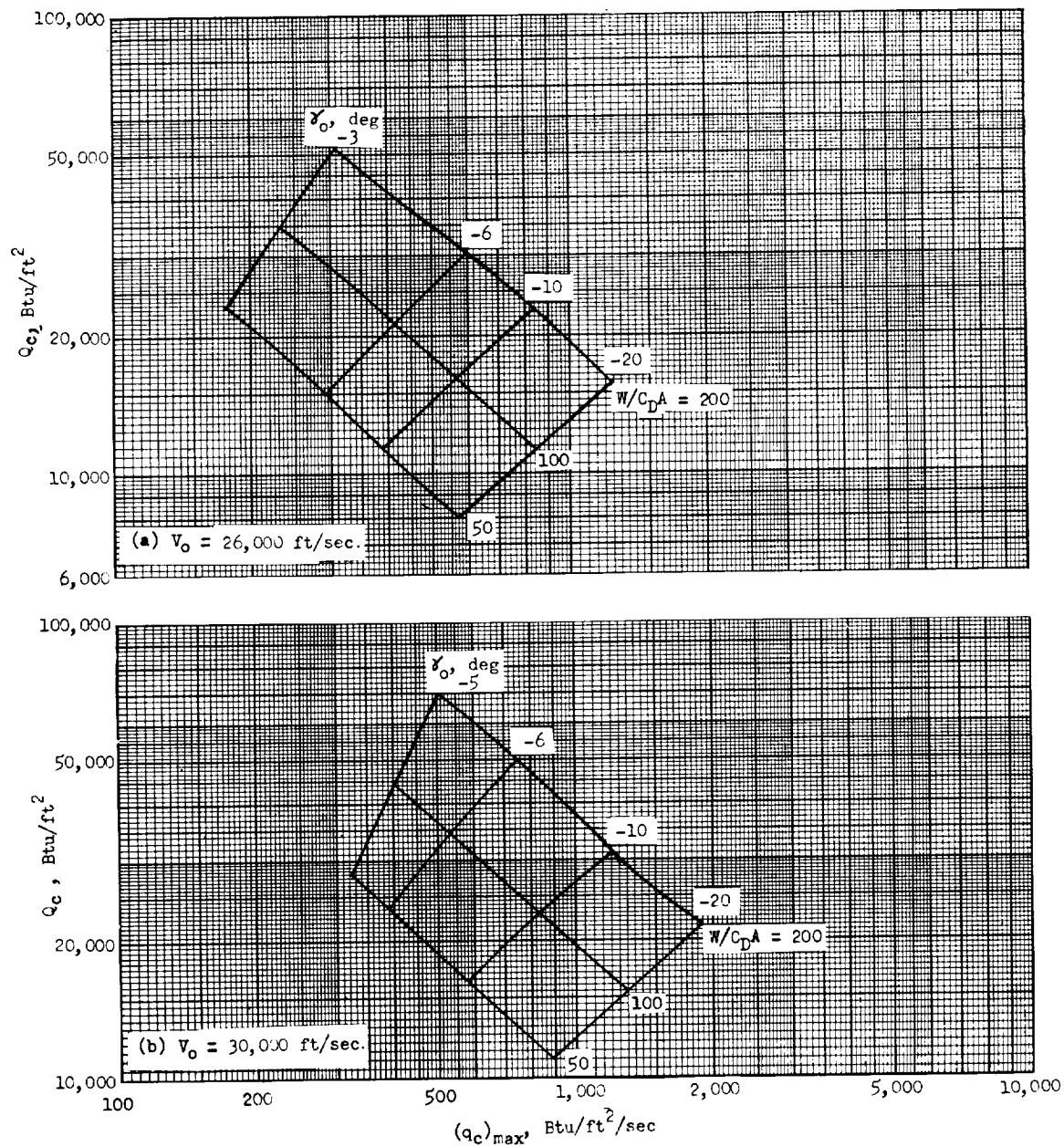


Figure 10.- Total convective heat input as a function of the maximum convective stagnation-point heating rate.

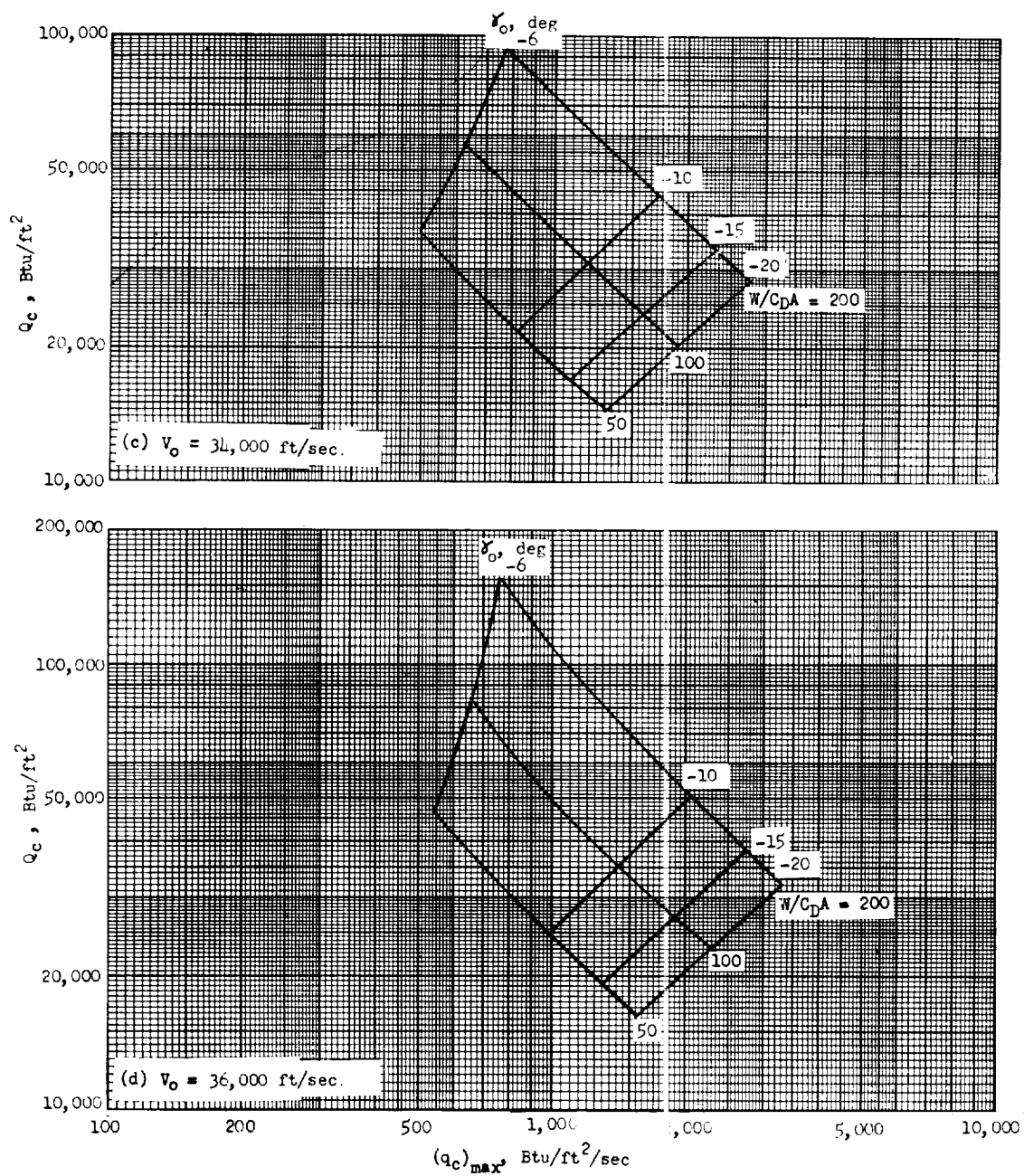


Figure 10.- Continued.

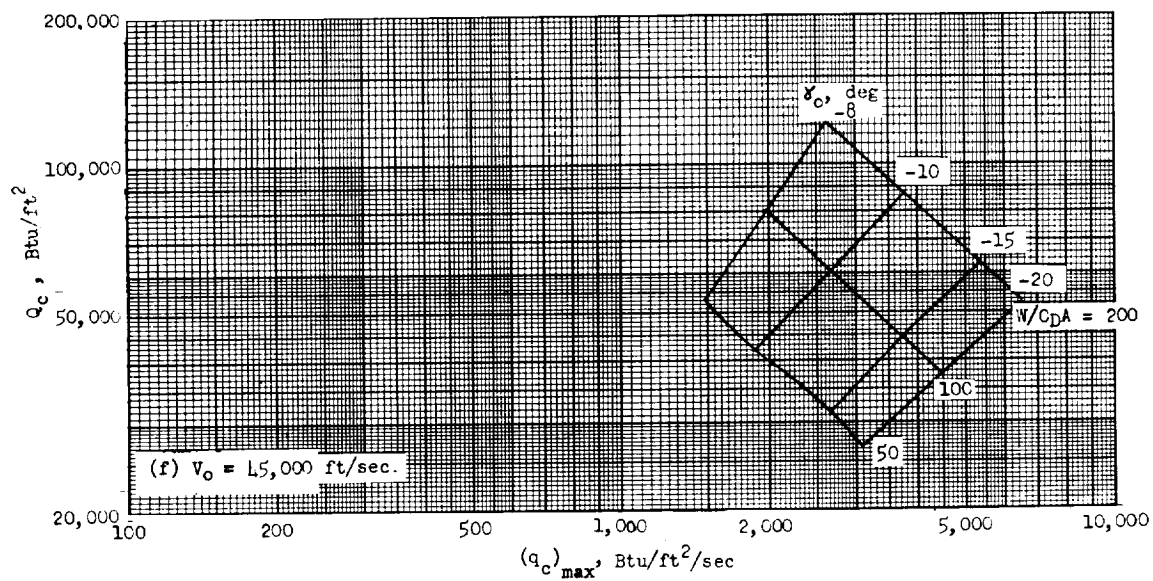
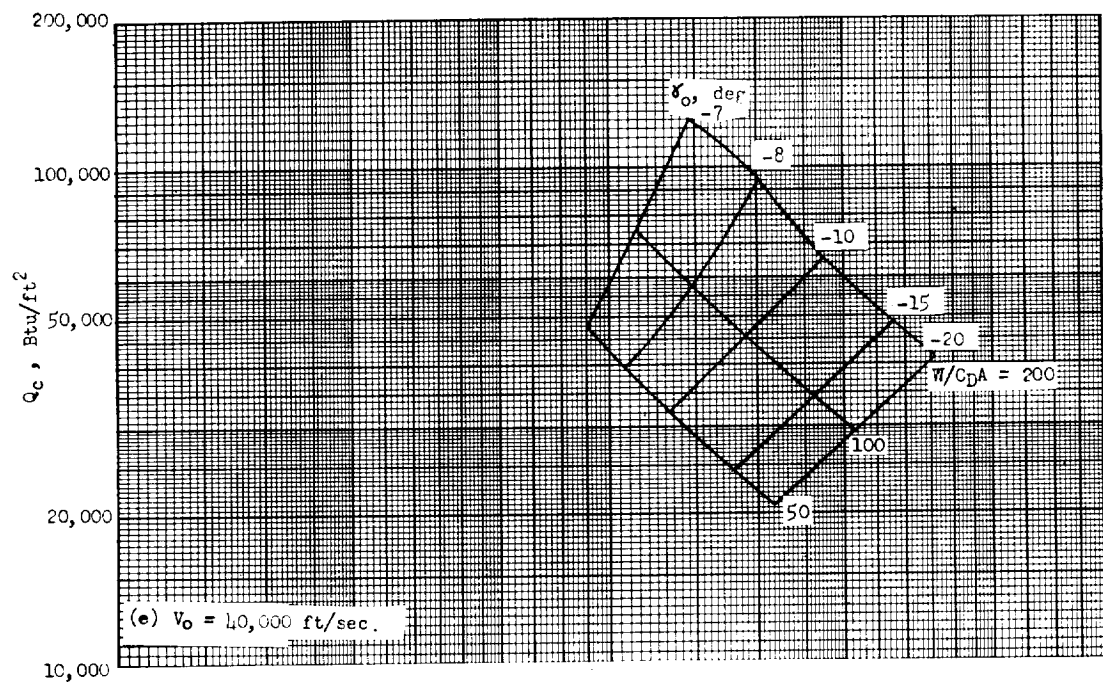


Figure 10.- Concluded.

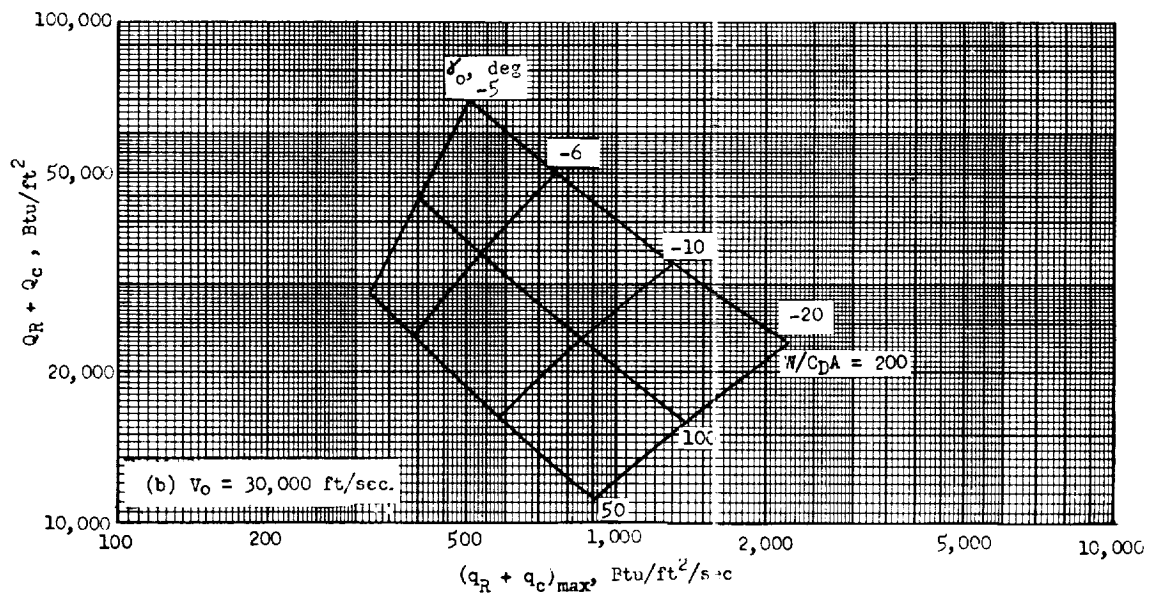
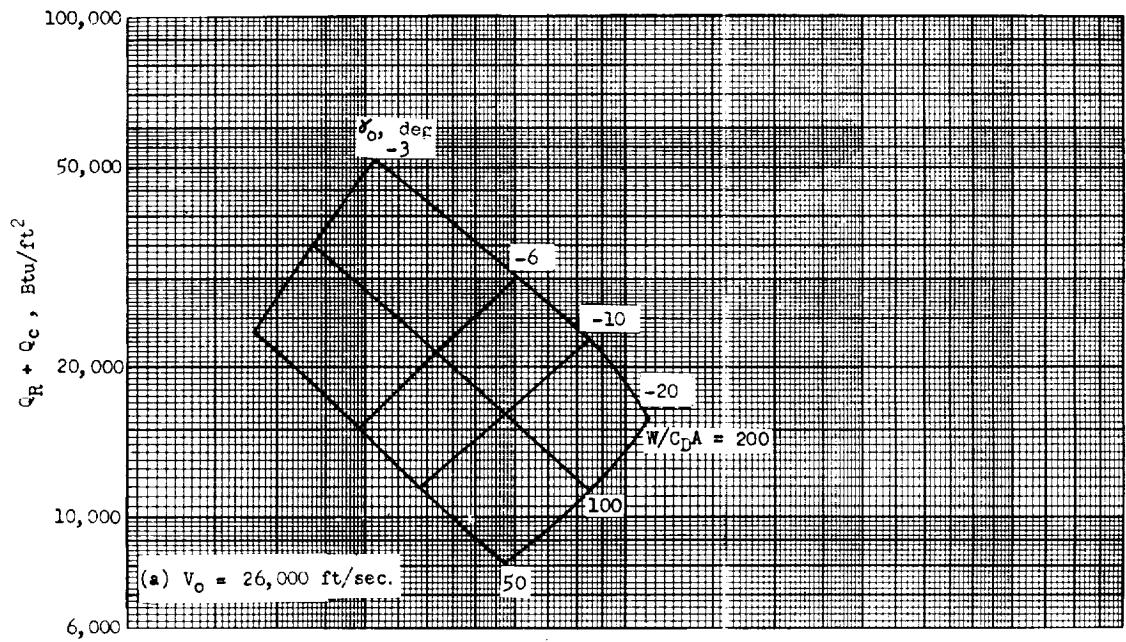


Figure 11.- Total heat input as a function of the maximum total stagnation-point heating rate.

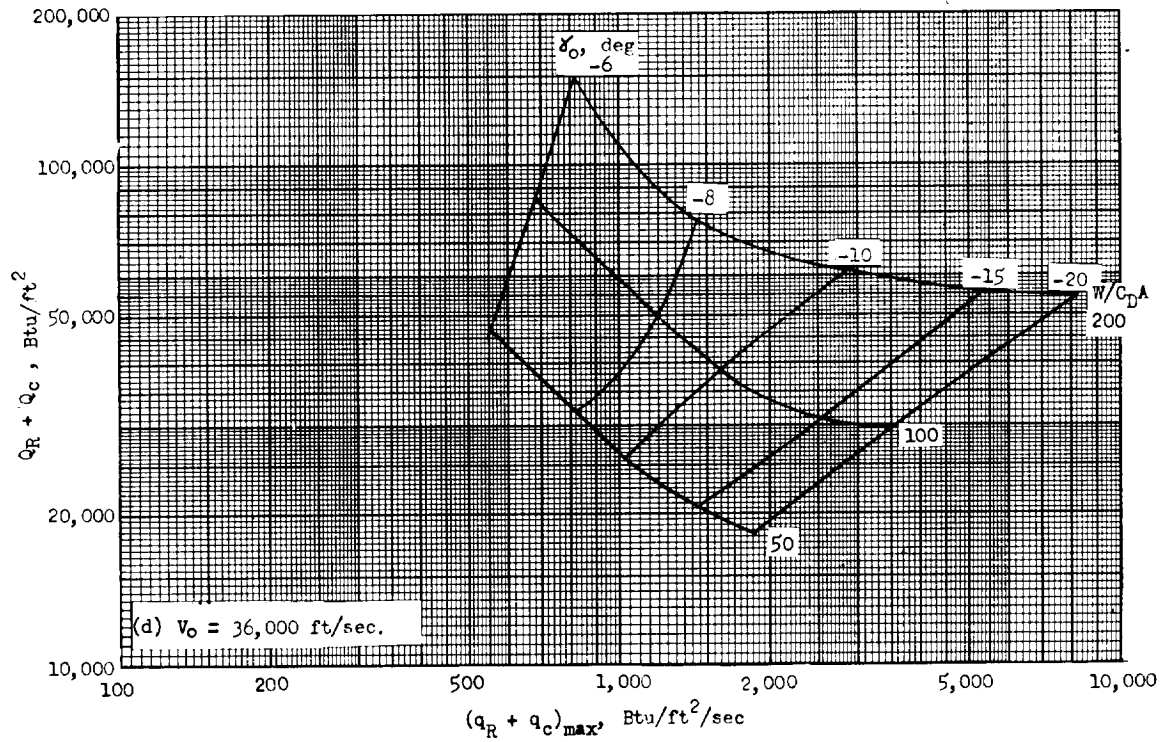
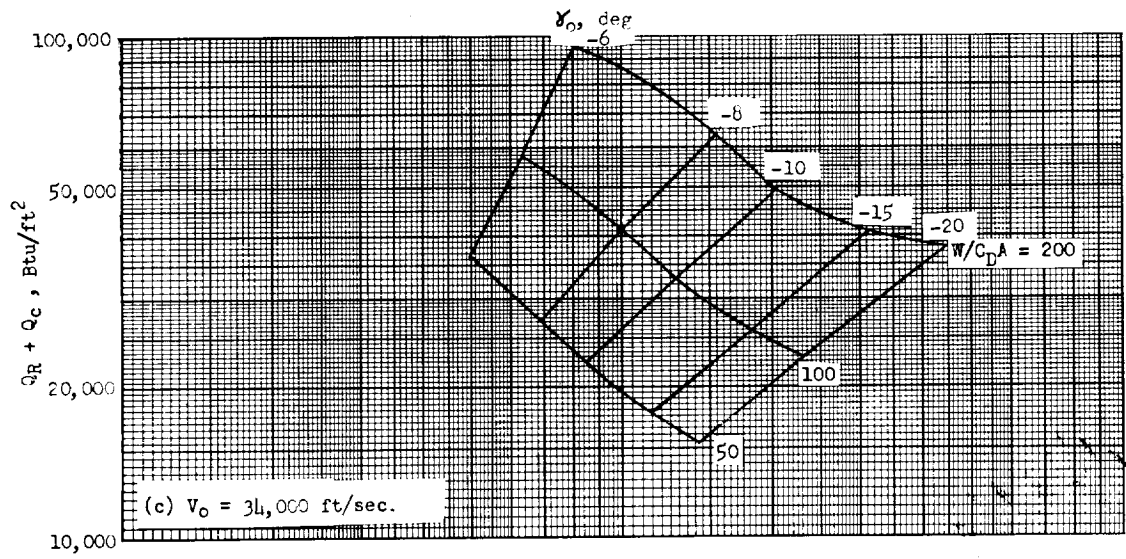


Figure 11.- Continued.

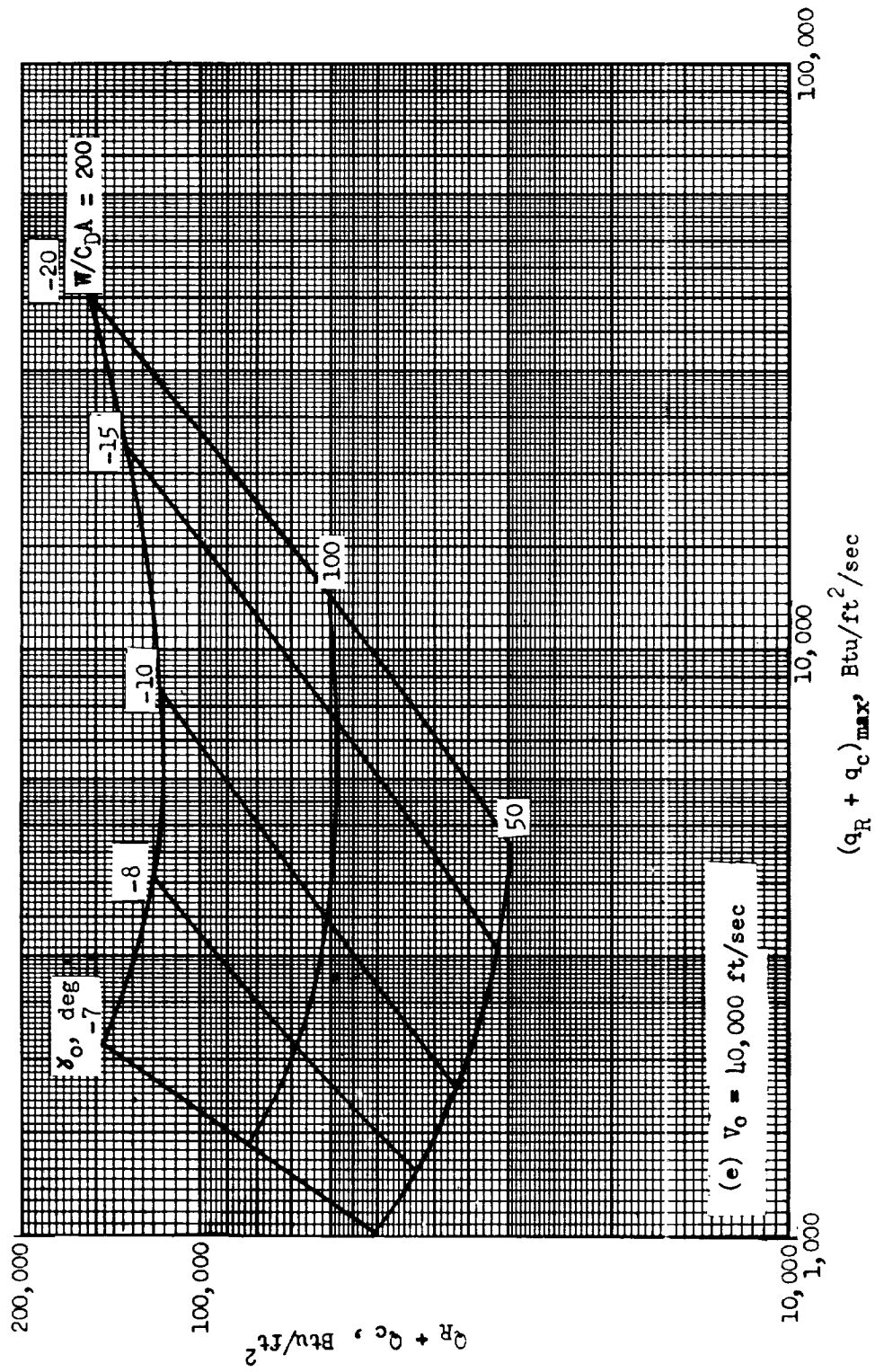


Figure 11.- Continued.

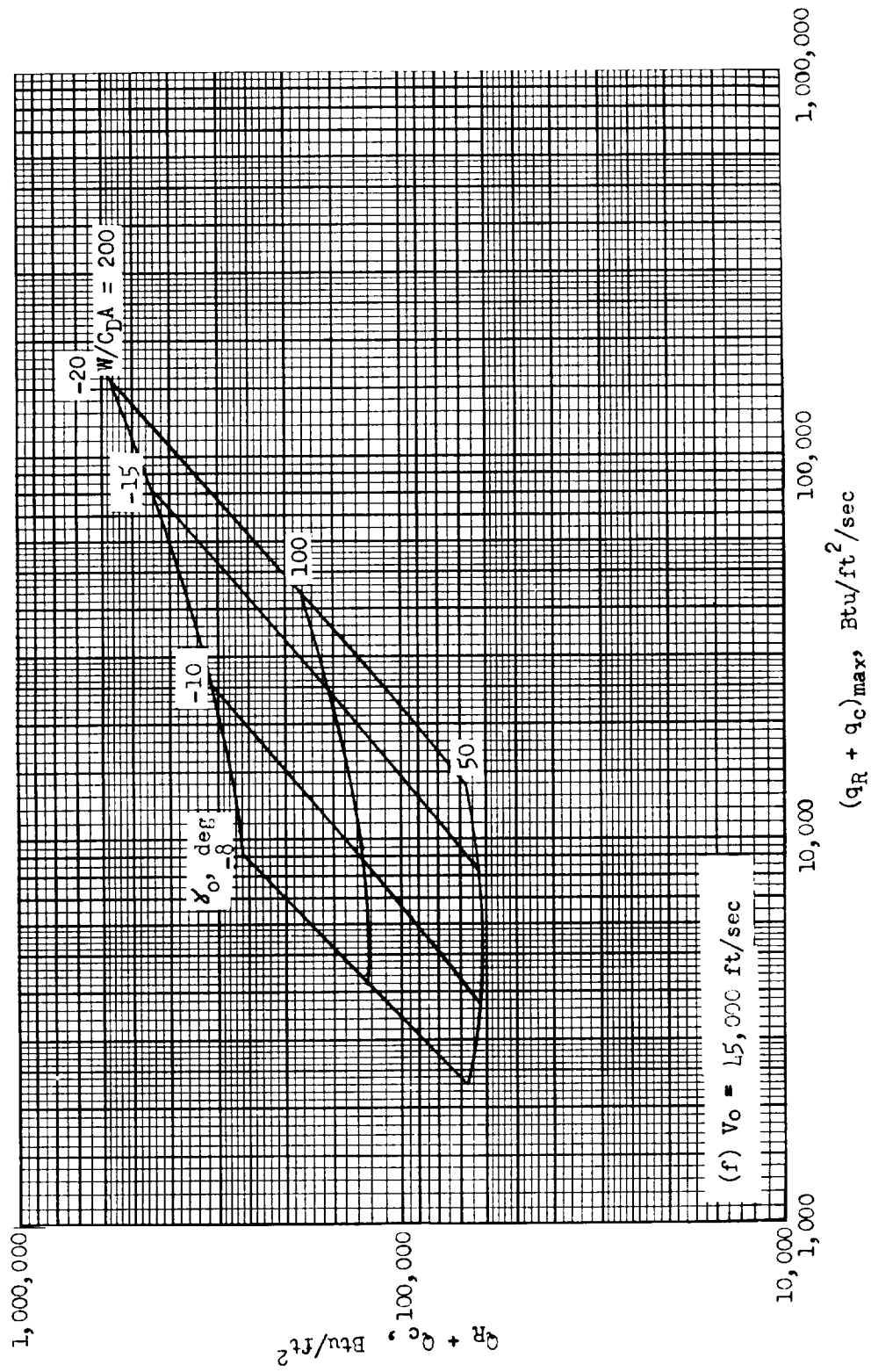
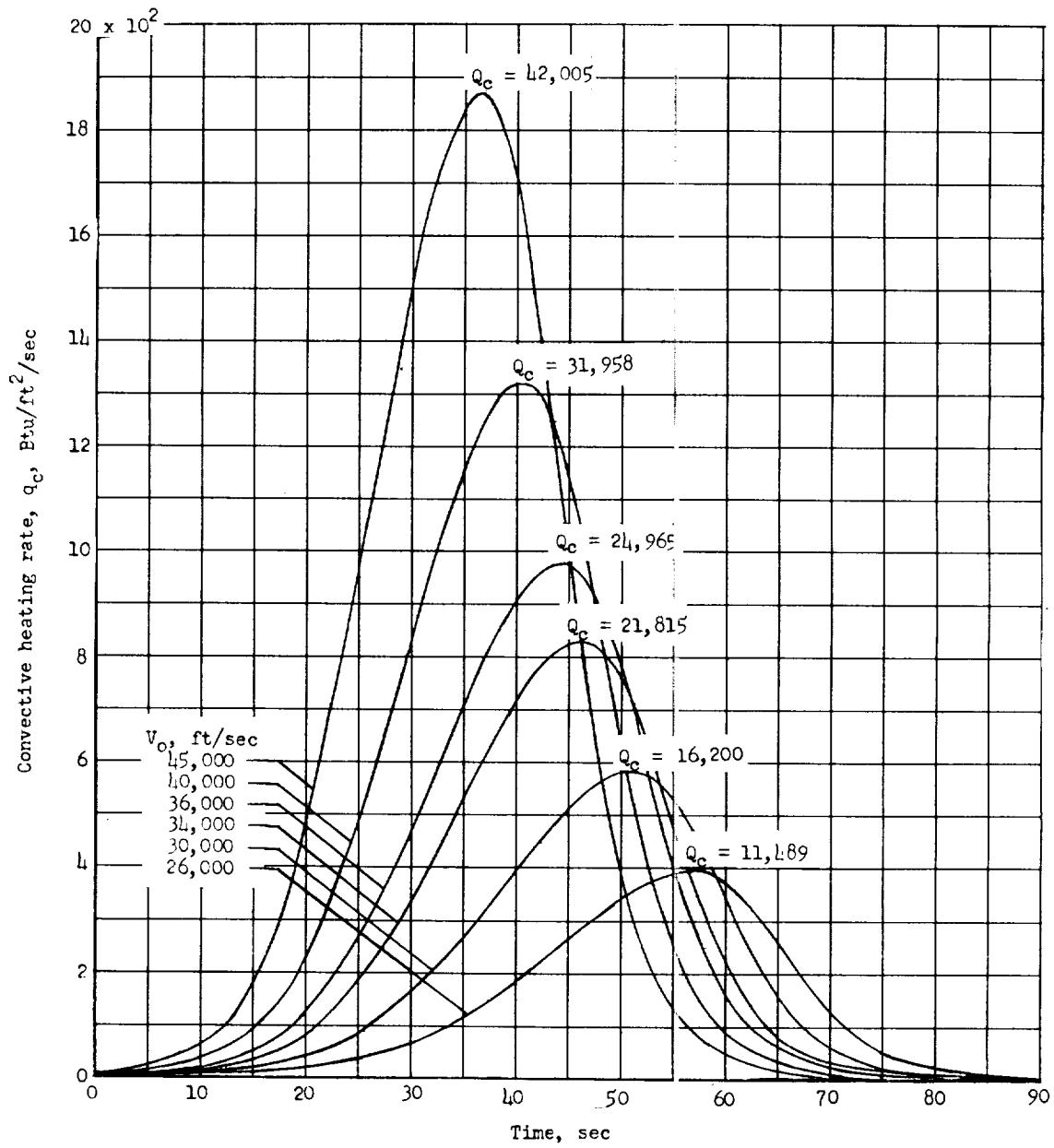


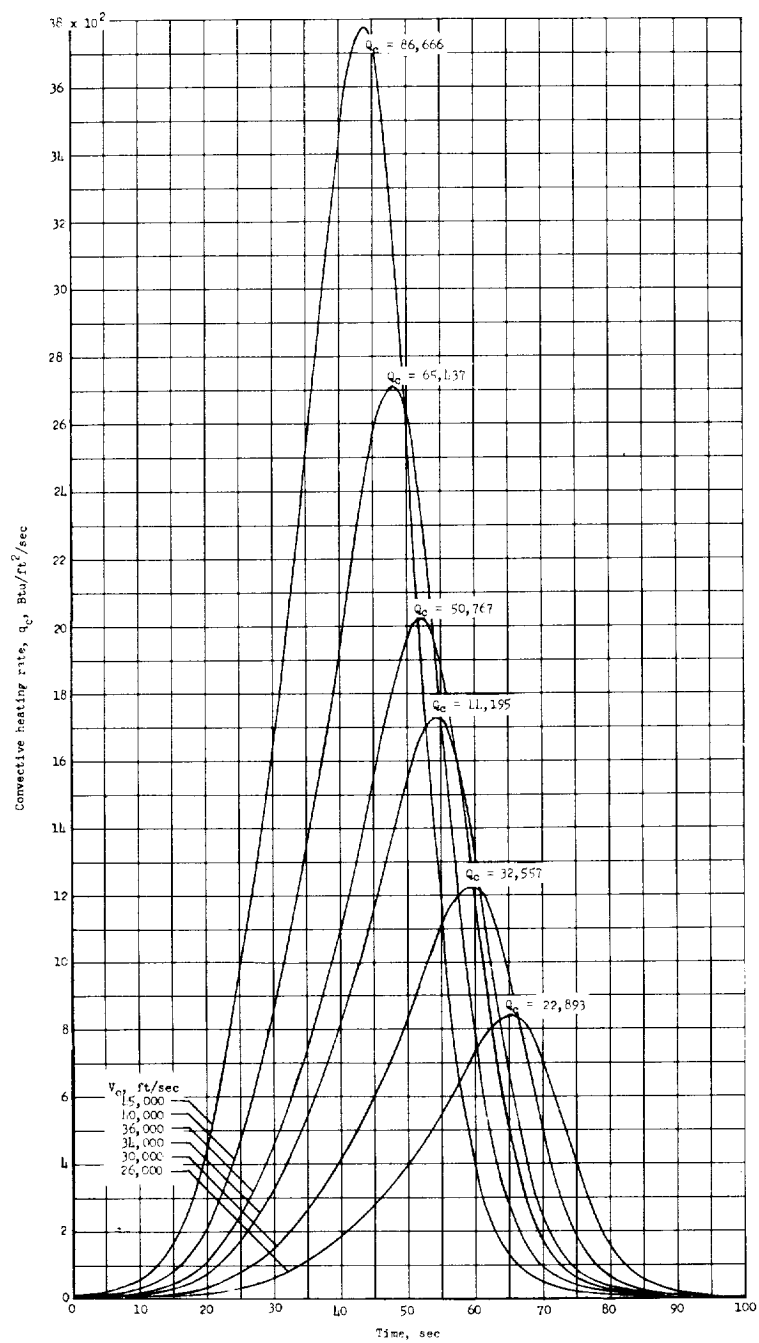
Figure 11.- Concluded.



(a) $\gamma_o = -10^\circ$; $\frac{W}{C_{DA}} = 50$.

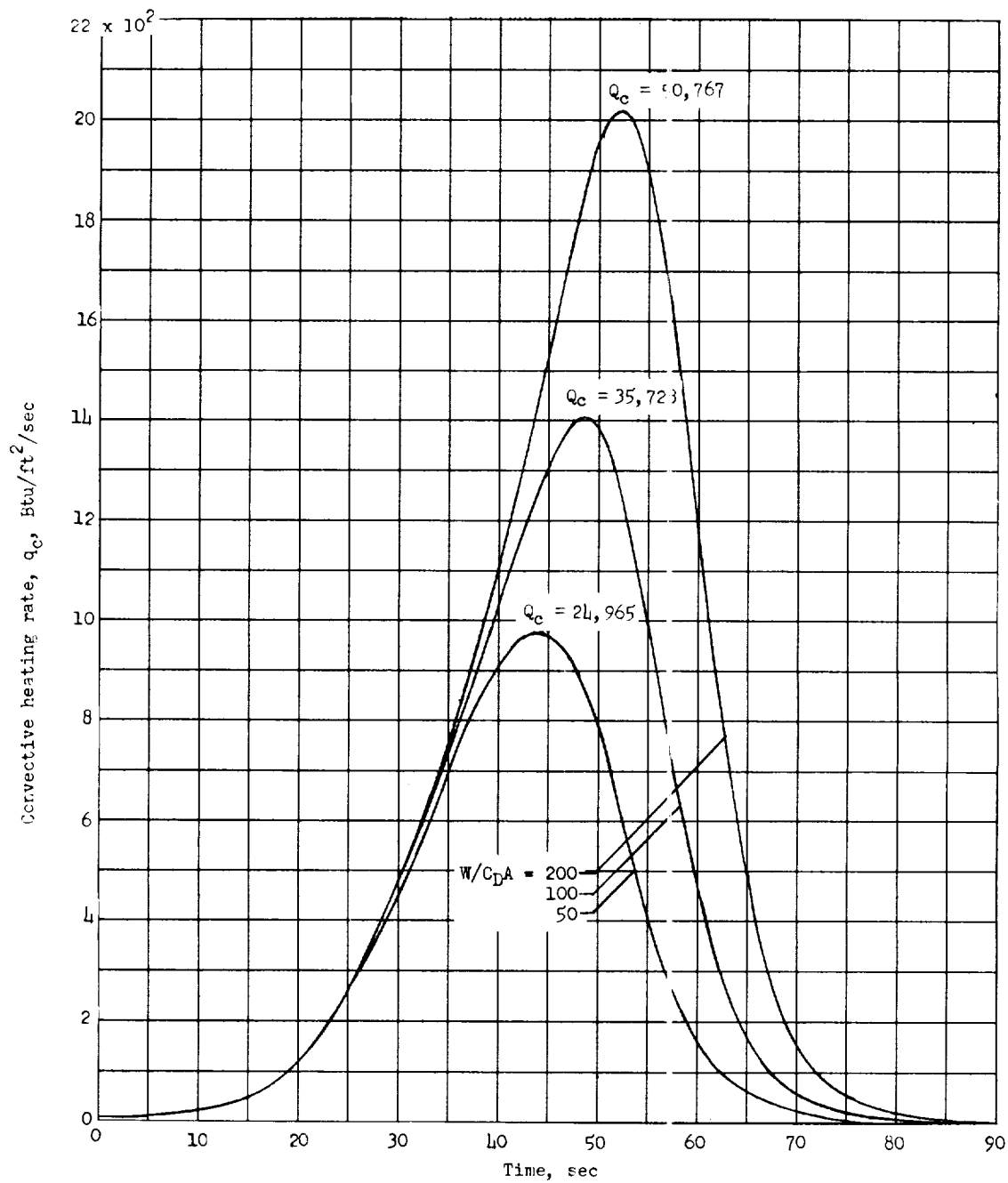
Figure 12.- Stagnation-point heating rate as a function of time.

L-1750



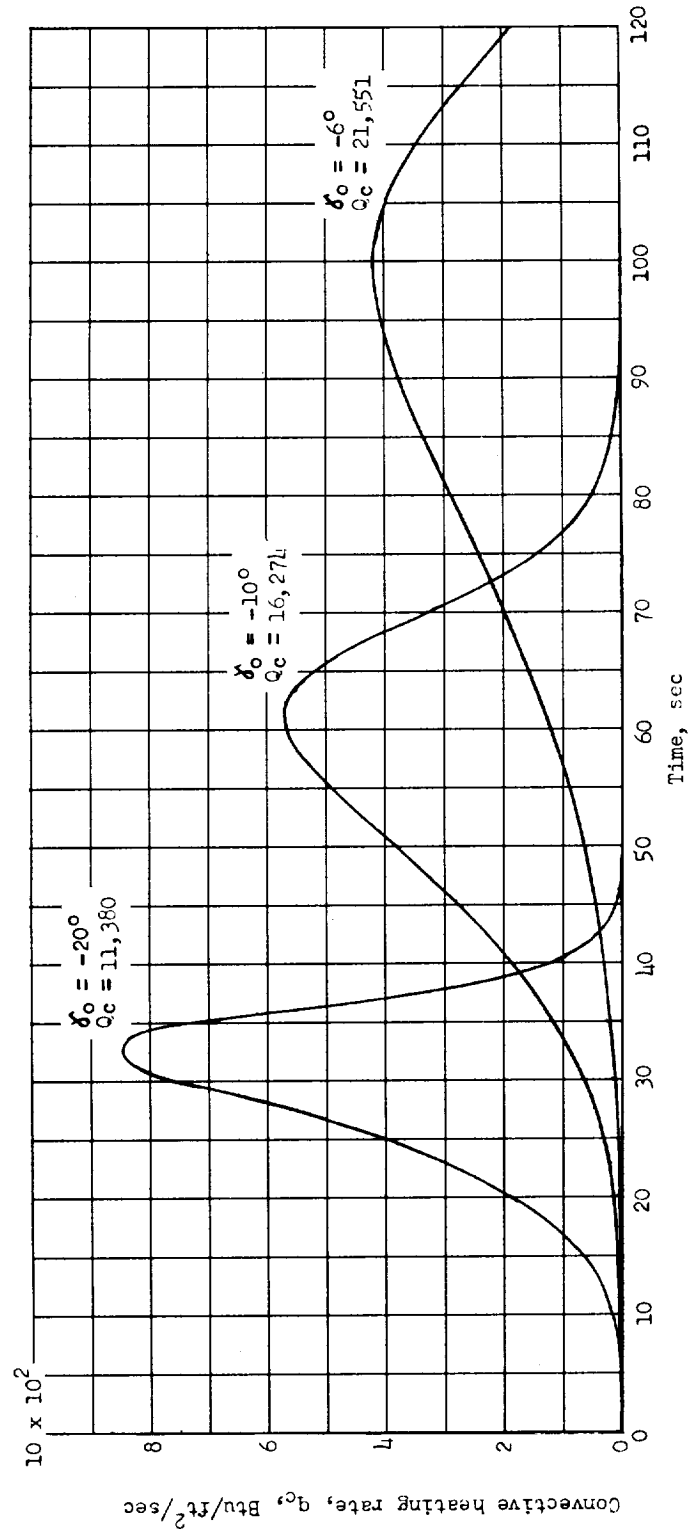
(b) $\gamma_0 = -10^\circ$; $\frac{W}{C_{DA}} = 200$.

Figure 12.- Continued.



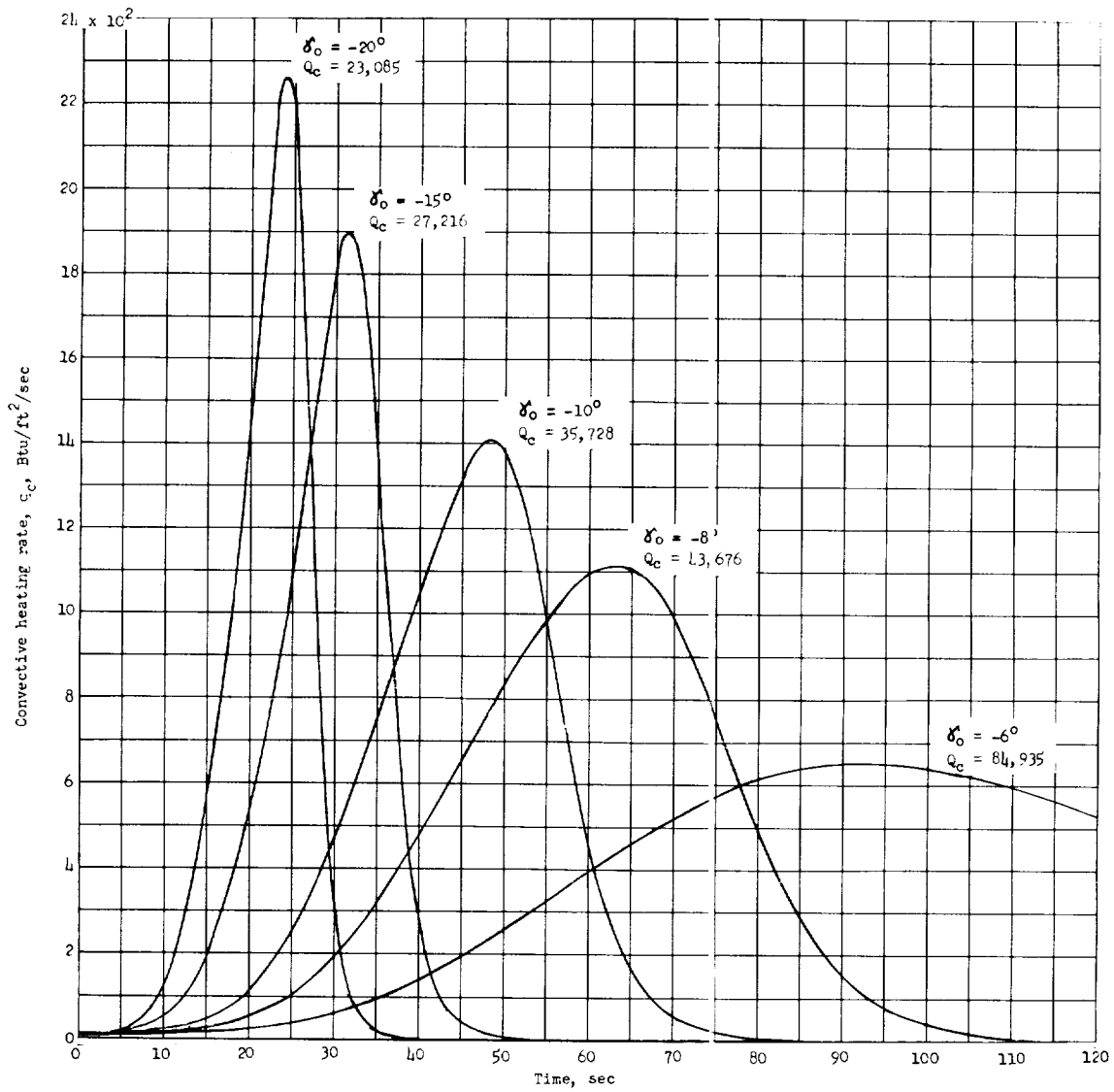
(c) $V_0 = 36,000$ feet per second; $\gamma_0 = -10^\circ$.

Figure 12.- Continued.



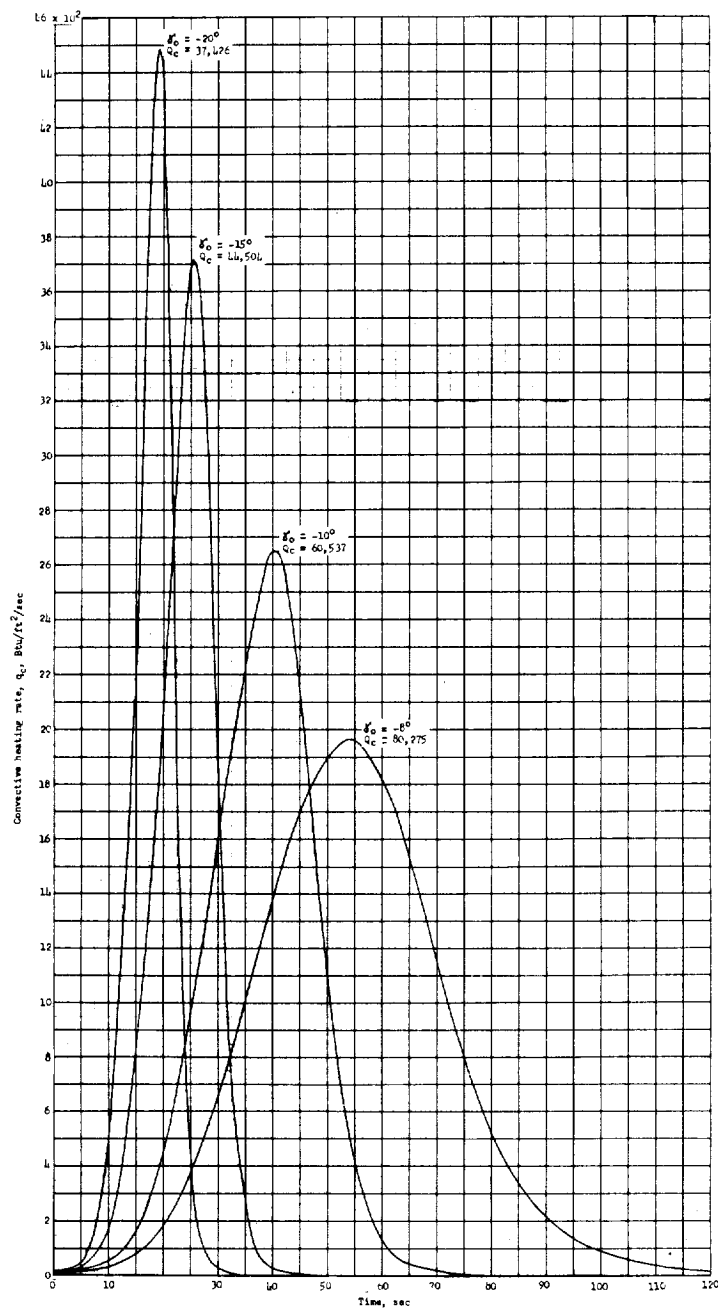
(d) $V_0 = 26,000$ feet per second; $\frac{W}{C_{DA}} = 100$.

Figure 12.- Continued.



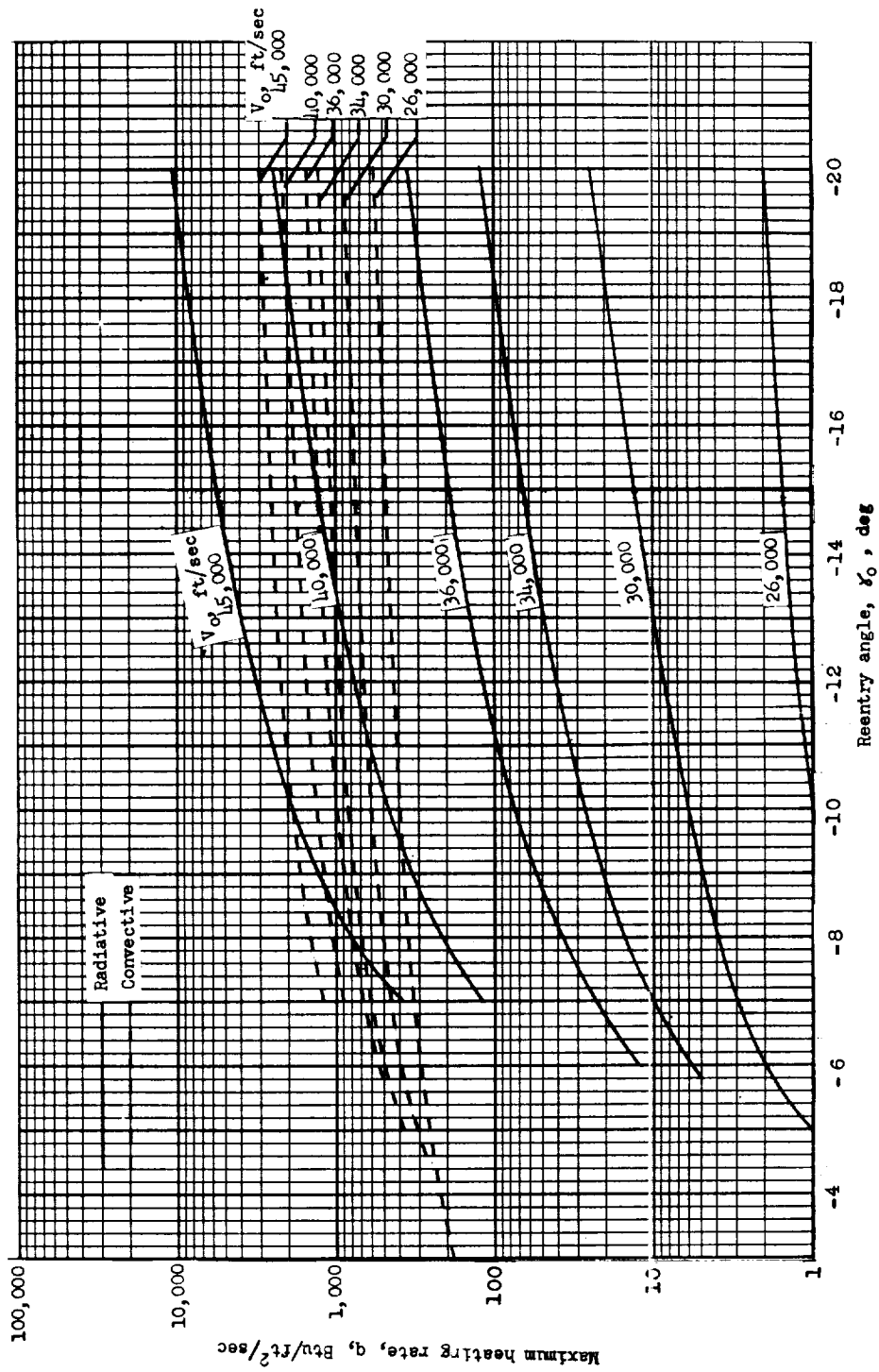
(e) $V_o = 36,000$ feet per second; $\frac{W}{C_D A} = 100$.

Figure 12.- Continued.



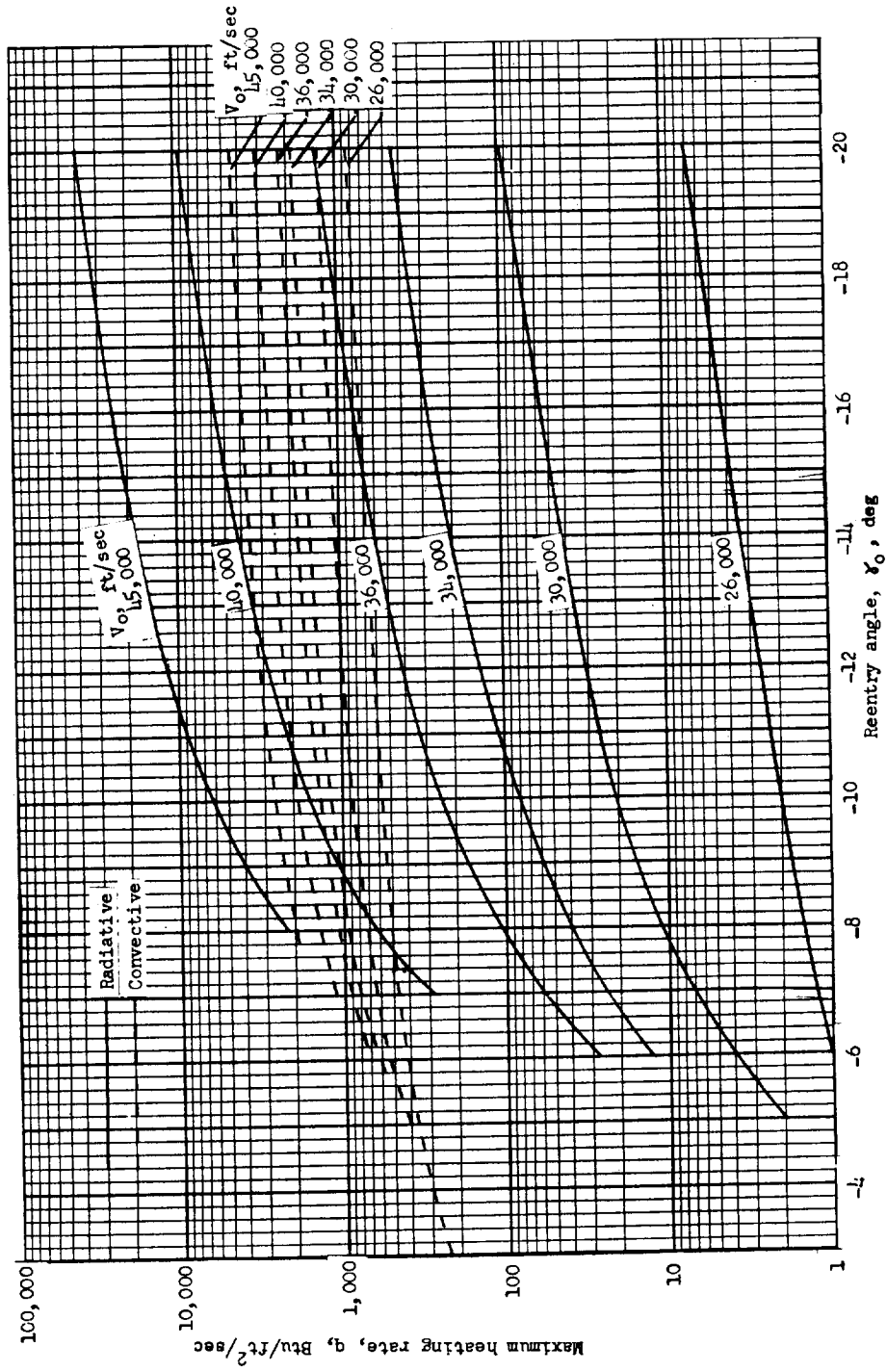
(f) $V_o = 45,000$ feet per second; $\frac{W}{C_{DA}} = 100$.

Figure 12.- Concluded.



$$(a) \quad \frac{W}{C_D A} = 50.$$

Figure 13.- Maximum heating rates.



(b) $\frac{W}{C_D A} = 100.$

Figure 13.- Continued.



(c) $\frac{W}{C_D A} = 200.$

Figure 13.- Concluded.